BULLETIN OF THE EARTHQUAKE
RESEARCH INSTITUTE
UNIVERSITY OF TOKYO
Vol. 62 (1987) pp. 19-59

Granular Assembly Simulation for Ground Collapse

Daisuke UEMURA* and Motohiko HAKUNO

Earthquake Research Institute

(Received October 31, 1986)

Abstract

The mechanical behavior of particle assemblies is described using the Cundall's distinct element method. This method is based on using an explicit numerical scheme. Particles interactions have been detected at every contact and particles motion has been modelled for every particle.

Using Cundall's simulation method, the present work aims at study in the mechanism of slope collapse, soil behaviors surrounding a pile penetrating the ground, non-linear dynamic response of structural foundation and the dynamic earth pressure of loose ground under vibrational excitations.

Results achieved using the model idealized as a continuous medium, which have been widely applied in the past, differ from those gained by using the granular assembly model adopted in this study. Ignoring the influence of movements of soil particles, including subsidence and rotation of particles, in the former method seems to be the cause of such differences.

1. Introduction

Soil dynamics are roughly classified, depending on the idealization of the medium, into continuous and discrete mediums. Handling the soil as a continuous body gives many results by employing the finite element method. Many unsolved problems still remain in the field of soil dynamics of the discrete medium.

Soil is basically a noncontinuous medium of numerous particles. Some phenomena such as rock avalanche, debris flow and dilatancy of soil can be clarified only by considering the soil as a discrete granular assembly. Therefore, the developing of a method to handle soil as a noncontinuous medium is necessary.

Soil handling methods, in the case of the noncontinuous medium, can be classified, according to what has been carried out in the field of soil dynamics, into three categories as follows:

1. Experiments using actual gravel and sand (ASHIDA *et al.*, 1982)

* Present address: Shimizu Construction Co. (Higashi Katsushika-gun, Chiba, Japan).

2. Experiments using many cylinders of lead or photoelastic materials, and
3. Computer simulation (CUNDALL, 1971)

In the first category, it is difficult to grasp the interior state of the assembly microscopically. Also, there are several restrictions concerning the principle of similarity. The difference between those materials used in the experiment and those of the actual soil became a problem in the second category. In the third category the model can be analyzed microscopically and also macroscopically using various material parameters such as the frictional coefficient. The limitation of particle numbers and the long computing time were the shortcomings of this method. New developments of the computer's capability overcome such obstacles.

In 1971, the Distinct Element Method (DEM) was introduced by Cundall (CUNDALL, 1971). The rock medium was considered as being the aggregate of an element which is divided by many discontinuous planes. This method analyzes the rock behavior numerically assuming that an individual rock element satisfies the equation of motion and the law of action and reaction. It is based on the use of an explicit numerical scheme in which the interaction of particles is monitored contact by contact. Cundall used this method to analyze the dynamics of two dimensional behavior of a rock particle assembly. KIYAMA and FUJIMURA (1983) applied Cundall's method to estimate the settlement of the ground surface during the construction of a tunnel assuming that the particles have a circular shape. They also analyzed the behavior of grain particles in a silo during their extrusion through a hole.

Having no idea whatsoever about Cundall's research, HIRAO and HAKUNO (1973) conducted the granular assembly simulation regarding the circular particles on the static deformation problem of sand. Due to the lack of time required to compute the equations for all particles simultaneously, they could only solve a static problem without deploying such approximation which was employed by Cundall and considering only those forces of particles' contact. The number of particles was approximately several hundreds, but CUNDALL (1979) mentioned that the maximum number of particles may be limited to one thousand owing to the computer capacity. These analyses were carried out using particle elements of similar radii and very low velocity.

The phenomena to be analyzed with simulation under such restrictions are limited and the merit of such a method is not sufficient if compared with the experimental method. Therefore, the authors modified Cundall's method by introducing a rebound coefficient and tried the dynamic analysis of a soil model of more than 3,000 circular

elements with different radii. Using circular elements also saves CPU time. Accordingly, such phenomena as the rock avalanche which occurred on Mt. Ontake due to the Naganoken Seibu earthquake in 1985, the soil behaviors during the penetration of a pile into the ground, the non-linear response of a structural foundation under a horizontal exciting load and the dynamic earth pressure to a retaining wall by ground motion could be analyzed successfully by using this method.

2. Distinct Element Method by Cundall

2.1 Distinct Element Method

CUNDALL'S (1971) Distinct Element Method (DEM) is based on the assumption that each element satisfies the equation of motion and that the transmission of force between the elements follows the law of action and reaction. This method is a new approach to analyze the dynamic behavior of granular assemblies numerically. In the early stage of the application of his method, CUNDALL (1971) assumed that the rock medium is an assembly of polygonal elements. It took a long time for computation due to the complicated judgement of the contact between particles. Therefore, the total number of elements used for the simulation was restricted by the limitation of CPU time. Later, he introduced the circular rather than the polygonal elements (CUNDALL *et al.*, 1979). In this case, each element is specified only by its radius. Therefore, it is easy to judge the contacts between elements and accordingly the computing time is reduced. The authors adopted the circular elements in order to increase the number of elements used in the simulation.

The motion of a particle having a mass m_i and a moment of inertia I_i is expressed as follows:

$$m_i \frac{d^2\boldsymbol{u}}{dt^2} + C_i \frac{d\boldsymbol{u}}{dt} + F_i = 0 \tag{2.1}$$

$$I_i \frac{d^2\varphi}{dt^2} + D_i \frac{d\varphi}{dt} + M_i = 0 \tag{2.2}$$

where F_i is the sum of all forces acting on the particle,
M_i is the sum of all moments acting on it,
C_i and D_i are the damping coefficients,
$\boldsymbol{u}$ is the displacement vector and φ is the angular displacement.

2.1.1 Evaluation of the Relative Displacement at Contact

For the two elements i (of a radius r_i) and j (of a radius r_j) in

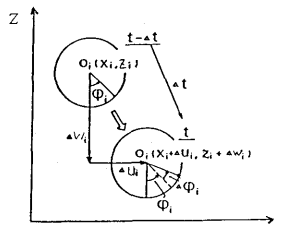

Fig. 2.1. Displacement increments and coordinates of elements i and j.

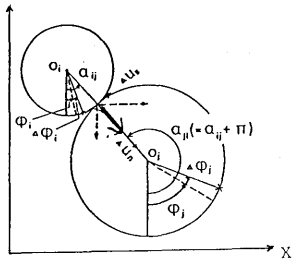

Fig. 2.2. Relative displacements at the contact.

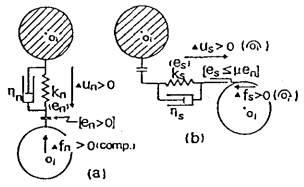

Fig. 2.3. Evaluation of the acting force at the contact.

Fig. 2.1, Δu_i and Δw_i are the X and Z components of the displacement increment. $\Delta\varphi_i$ is the rotational increment, and Δt is an infinitesimal time increment. Fig. 2.2 shows the case where element i approaches element j. The condition of the state of contact is

$$r_i+r_j \leqq R_{ij} \tag{2.3}$$

where,

$$R_{ij}=\sqrt{(X_i-X_j)^2+(Z_i-Z_j)^2}$$

(X_i, Z_i) indicates the X and Y coordinates of the center of element i.

If α_{ij} is positive in the counterclockwise direction, we obtain the following equations as an index of the contacting point

$$\sin\alpha_{ij}=(Z_i-Z_j)/R_{ij} \tag{2.4.a}$$
$$\cos\alpha_{ij}=(X_i-X_j)/R_{ij} \tag{2.4.b}$$

The relative displacement increment in the normal direction Δu_n (approach is considered positive) and the relative displacement increment in the tangential direction Δu_s (positive in counterclockwise direction) between the two contacting elements i and j during Δt can be calculated as follows:

$$\Delta u_n=-(\Delta u_i-\Delta u_j)\cos\alpha_{ij}-(\Delta w_i-\Delta w_j)\sin\alpha_{ij} \tag{2.5.a}$$
$$\Delta u_s=(\Delta u_i-\Delta u_j)\sin\alpha_{ij}-(\Delta w_i-\Delta w_j)\cos\alpha_{ij}+(r_i\Delta\varphi_i+r_j\Delta\varphi_j) \tag{2.5.b}$$

2.1.2 Evaluation of the Acting Forces at the Contact

As shown in Fig. 2.3 (a), the acting force is divided at the contacting plane of elements i and j into two components: a compressional force f_n acting in the normal direction and a shear force f_s acting in the tangential direction.

i) Force Acting in the Normal Direction

An elastic spring between particles should be introduced in order to estimate the force, which has been produced by other contacting particles, acting on a certain particle. The acting force can't be estimated using the law of equilibrium of force only. Particles' deformation should also be considered in case of three or more contacting particles.

CUNDALL (1979) assumed a parallel disposition of an elastic spring (constant K_n) and a viscous dashpot (η_n). This elastic spring causes Δe_n, which is the force proportional to Δu_n: the relative displacement increment during Δt as shown in Fig. 2.2. This viscous dashpot causes a reactional force Δd_n proportional to $\Delta u_n/\Delta t$, which is the relative velocity, i.e.

$$\Delta e_n = K_n \Delta u_n \tag{2.6.a}$$

$$\Delta d_n = \eta_n \Delta u_n / \Delta t \tag{2.6.b}$$

where the compressional force is positive.

The elastic reaction force $[e_n]_{t+\Delta t}$ and the viscous reaction force $[d_n]_{t+\Delta t}$ acting in the normal direction at time $t+\Delta t$ are:

$$[e_n]_{t+\Delta t} = [e_n]_t + \Delta e_n \tag{2.7.a}$$

$$[d_n]_{t+\Delta t} = \Delta d_n \tag{2.7.b}$$

This viscous dashpot was introduced in Cundall's DEM to prevent the instability of the numerical computation.

However, the dashpot was not applied in this study because of the difficulty of estimating the viscosity value. The rebound coefficient was introduced at the particles' collision in order to dissipate the system's energy, as previously mentioned. This can simulate the observed (real) behavior well.

We cannot consider a tensional reaction force between particles since the tension joint hasn't been taken into consideration. An additional condition has been attached to the equation 2.7,

when $[e_n]_t < 0$

$$[e_n]_t = [d_n]_t = 0 \tag{2.8}$$

The compressional force acting in the normal direction between the two elements at time t is calculated as

$$[f_n]_t = [e_n]_t + [d_n]_t \tag{2.9}$$

ii) Force Acting in the Tangential Direction

Cundall assumed that the elastic spring (K_s) and viscous dashpot (η_s) are parallel to each other (Fig. 2.3.(b).) This elastic spring causes

a force Δe_s proportional to Δu_s and the viscous dashpot causes a reactional force Δd_s proportional to $\Delta u_s/\Delta t$. The increments of the elastic reactional force and the viscous reactional force are

$$\Delta e_s = K_s \cdot \Delta u_s \tag{2.10.a}$$

$$\Delta d_s = \eta_s \cdot \Delta u_s / \Delta t \tag{2.10.b}$$

The elastic reactional force $[e_s]_{t+\Delta t}$ and viscous reactional force $[d_s]_{t+\Delta t}$ acting in the tangential direction at $t+\Delta t$ are:

$$[e_s]_{t+\Delta t} = [e_s]_t + \Delta e_s \tag{2.11.a}$$

$$[d_s]_{t+\Delta t} = \Delta d_s \tag{2.11.b}$$

Here, two more conditions are added; if

$$[e_n]_t \leqq 0$$

then

$$[e_s]_t = [d_s]_t = 0 \tag{2.12}$$

and if

$$|[e_s]_t| > \mu [e_n]_t$$

then

$$[e_s]_t = \mu [e_n]_t \cdot \mathrm{sign}([e_s]_t) \tag{2.13.a}$$

$$[d_s]_t = 0 \tag{2.13.b}$$

where μ is the friction coefficient between particles.

These conditions indicate that the shear deformation is caused by the frictional force between elements near the contacting point. Equation 2.12 corresponds to the no contact condition and equation 2.13 shows the limitation of the frictional force.

The shear force $[f_s]_t$ (positive in clockwise direction) between two elements in a tangential direction at time t is calculated by

$$[f_s]_t = [e_s]_t + [d_s]_t \tag{2.14}$$

iii) Approximate Solution for the Differential Equation of Motion

Once we obtained the forces of contact $[f_n]_t$ and $[f_s]_t$ using equations 2.9 and 2.14 for all elements contacting with element i, we can calculate the resultant forces in both directions X and Z: FX_i, FZ_i and the resultant moment M_i at the center of i (positive in counterclockwise direction) by using the following equations:

$$[FZ_i]_t = \sum_j ([f_n]_t \sin \alpha_{ij} + [f_s]_t \cos \alpha_{ij}) - m_i g \tag{2.15.a}$$

$$[FX_i] = \sum_j ([f_n]_t \cos \alpha_{ij} + [f_s]_t \sin \alpha_{ij}) \tag{2.15.b}$$

$$[M_i]_t = -r_i \sum_j ([f_s]_t) \tag{2.15.c}$$

$\sum_j$ represents the sum of all j elements contacting with element i, m_i is the mass of element i and g is the gravity acceleration taken in the negative direction of z.

By obtaining the acting forces, the accelerations at time t can be defined by applying Newton's second law

$$[\ddot{u}_i]_t = [FX_i]_t / m_i \tag{2.16.a}$$
$$[\ddot{w}_i]_t = [FZ_i]_t / m_i \tag{2.16.b}$$
$$[\ddot{\varphi}_i]_t = [M_i]_t / I_i \tag{2.16.c}$$

where I_i is the moment of inertia of element i and m_i is its mass.

Integrating the above equations, we obtain the velocities at t;

$$[\dot{u}_i]_t = [\dot{u}_i]_{t-\Delta t} + [\ddot{u}_i]_t \cdot \Delta t \tag{2.17.a}$$
$$[\dot{w}_i]_t = [\dot{w}_i]_{t-\Delta t} + [\ddot{w}_i]_t \cdot \Delta t \tag{2.17.b}$$
$$[\dot{\varphi}_i]_t = [\dot{\varphi}_i]_{t-\Delta t} + [\ddot{\varphi}_i]_t \cdot \Delta t \tag{2.17.c}$$

and if we integrate the above equations, we obtain the displacement increments at time t;

$$[\Delta u_i]_t = [\dot{u}_i]_t \cdot \Delta t \tag{2.18.a}$$
$$[\Delta w_i]_t = [\dot{w}_i]_t \cdot \Delta t \tag{2.18.b}$$
$$[\Delta \varphi_i]_t = [\dot{\varphi}_i]_t \cdot \Delta t \tag{2.18.c}$$

These new values for the displacement increments are used in the force-displacement law and then we repeat the cycle from equation 2.5 to equation 2.18 for a new time increment.

The calculations performed in the Distinct Element Method were consecutively repeated through the force-displacement law and the law of motion at the contacts. The force-displacement law is applied at every contact of any element. The contacting forces acting in the normal and tangential directions are determined to yield to the resultant force acting on that element. After completing that procedure for an element of the assembly, new accelerations have been calculated using the law of motion. Thus, the displacement increments have been obtained.

iv) Collision of Particles

After the collision of particles there is a possibility of having a high velocity of motion. Also, we ignore the damping force. Such high velocity does not exist in the actual phenomena of rock collisions. Therefore, a rebound coefficient K has been introduced for velocities higher than V_0.

In most cases the values of K, K_n, K_s and V_0 are taken as 0.1, 1.0×10^6 (N/m), 3.0×10^5 (N/m) and 1.0 (m/sec) respectively.

3. Simulation of Slope Collapse

A large-scale slope collapse occurred at the time of Naganoken Seibu earthquake on 14, September 1984. That collapse spanned several kilometers and caused great damage to nearby houses, etc. The mechanism of such debris flow should be cleared in order to be applied to the field of earthquake disaster prevention. Also, it becomes inevitable to analyze soil idealized as an assembly of discrete rock particles.

In the present study a simulation of a slope, based on Cundall's model, was carried out under the assumption of having a granular nature.

3.1 Setting of Models

The collapsed slope on Mt. Ontake is illustrated in Figs. 3.1 and 3.2. Debris flowed straight down almost from the peak towards the valley of the Denjyo river where it crossed the stream and ran uphill. This collapse was simulated with a two dimensional model as follows:

(1) The cross section of the collapsed slope is approximated by seven straight lines as shown in Fig. 3.3.

(2) We assumed that a hole (A in Fig. 3.3), which simulates the

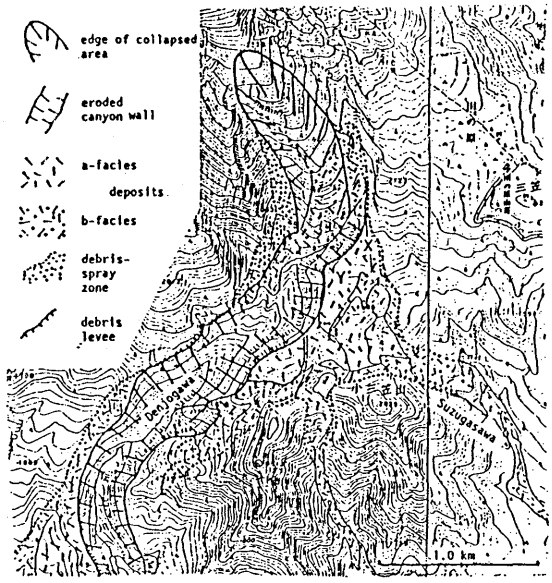

Fig. 3.1. Collapse of the slope of Mt. Ontake.

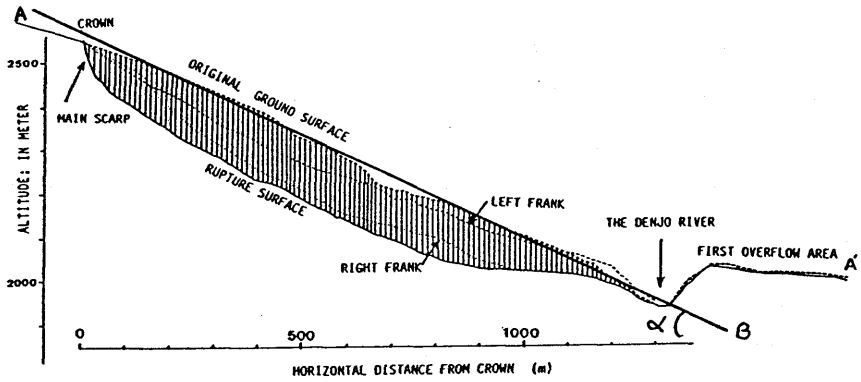

Fig. 3.2. Longitudinal section of Mt. Ontake landslide.

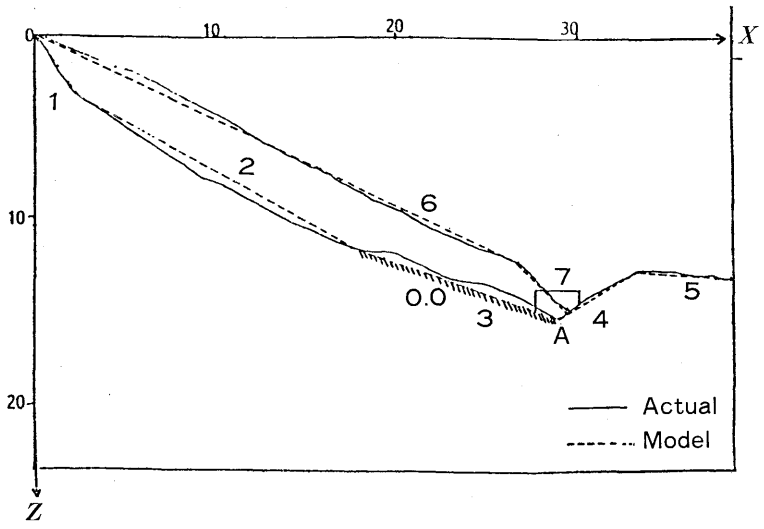

Fig. 3.3. Seven lines to model the collapsed cross-section of Mt. Ontake.

70 m wide Denjo river, was opened ten seconds after the start of the debris flow. It opened the way for rock particles to fall down free, i.e. they fell down in the valley. This assumption was made to give the same effect of debris flow in the three dimensional model. The maximum radius of rock grains on Ontake's collapsed slope was considered to be approximately 25 m according to an eyewitness. Rock grains with a radius less than 25 m were assumed to be uniformly distributed. A frame was built with a shape similar to the collapsed slope and packed full with 340 particles. Particles were then allowed to slide down resembling the collapse. Fig. 3.4 shows the distribution of the radii of the 340 particles. An external force was applied on the mountain slope model to simulate the cause of slope fracture.

The bed rock of the collapsed slope consists mainly of breccia.

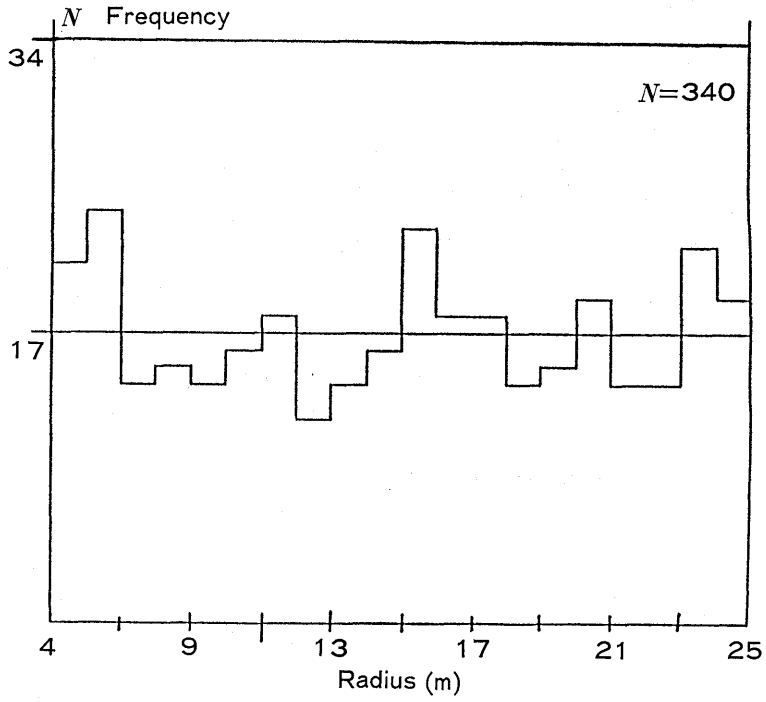

Fig. 3.4. Radius distribution of particles.

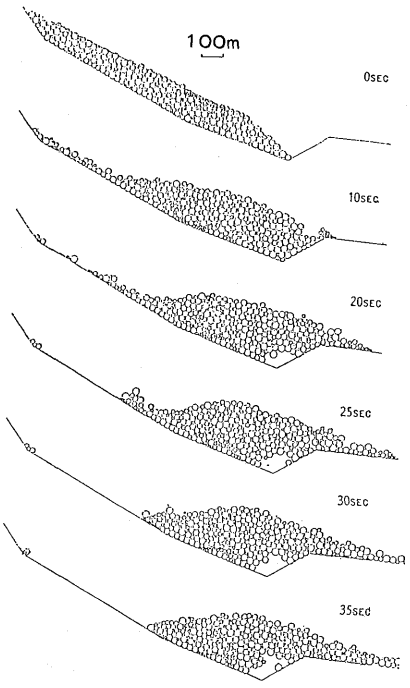

Fig. 3.5. Sliding particles of Mt. Ontake slope.

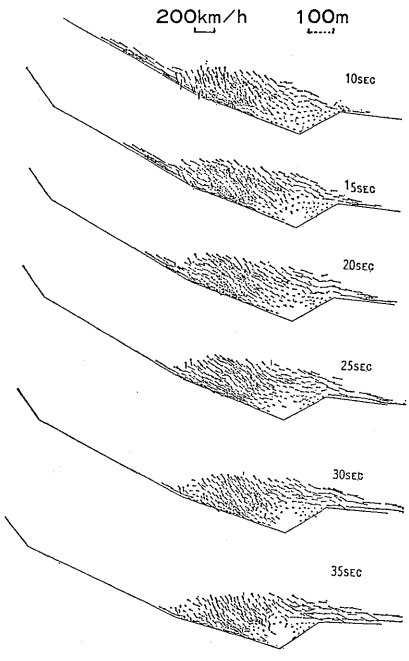

Fig. 3.6. Particles velocity of sliding Mt. Ontake slope.

The geological section of the collapsed slope shows that the bed rock was overlaid by a 50 cm thick layer of volcanic ash mixed with pumice and breccia fragments. A scoria layer, one to two meters thick, covered that layer. A volcaniclastic layer more than ten meters thick overlaid that scoria layer. The bottom layer which was a mixture of volcanic ash, pumice and breccia fragments extended along the slope having the shape of the buried valley. Its porous nature led to high water content. Accordingly, the large scale landslide on Mt. Ontake ought to be due to the liquefaction phenomenon of this layer which was activated by an earthquake shock. An equivalent trigger effect on the slope model was induced by suddenly changing the friction coefficient between liquefied rock particles to zero instead of applying a direct seismic loading.

3.2 Simulation Results

The position of each particle every 5 or 10 seconds is shown in Fig. 3.5. The velocity distribution of each particle is shown in Fig. 3.6 The particles that slipped into the Denjou river are not shown.

3.3 Inferences

Figs. 3.5 and 3.6 illustrate that the rock debris flowed down with a surface similar to a sine wave. Large particles accumulated at the flow's toe. In previous real collapses of slopes such large blocks of rocks concentrated at the flow's toe causing lots of damage. This might be due to the greater rotational speed of large particles.

A witness said that the highest speed of the rock debris flow during the collapse was approximately 100 km/h. However, the analytical estimation showed the highest speed to be about 200 km/h. There was no significant difference between the speed at the flow's top and that at the toe. The difference between the actual and the analytical speed is related to the resistant forces of air on particles which were not considered in the analysis.

4. Soil Behavior Surrounding a Pile Penetrating into the Ground

Practically when a structure penetrates the soil, soil particles move. Many studies have been conducted regarding such penetrations in a plastic continuous domain. The plastic discontinuous domain has not been considered so much. Studies on these kinds of problems have not been performed because such movement of soil particles cannot be handled through the analysis conducted for a conventional continuous medium. In the present study, a simulation was performed

considering the soil as an assembly of soil particles related to a pile penetrating the ground.

4.1 Simulation Results

Two types of vertical forces were applied to a pile, as shown in Fig. 4.1. The first type is called an A-type force which is monotonously increasing and the second force consists of an A-type plus sinusoidal. Table 4.1 gives the various cases of numerical simulations. Simulation results are shown in Figs. 4.2 to 4.7. The small spots in Fig. 4.6 indicate the initial location of the center of particle. Several typical examples of locations, velocity distributions and normal force distribution of particles in six cases are shown in Figs. 4.2 to 4.5. The compressive normal forces are indicated by solid lines and the tensile forces by double solid lines. The length of each line is proportional to the force's amplitude. Fig. 4.6 illustrates the loci of particles during penetration and Fig. 4.7 shows the speed of penetration in each case.

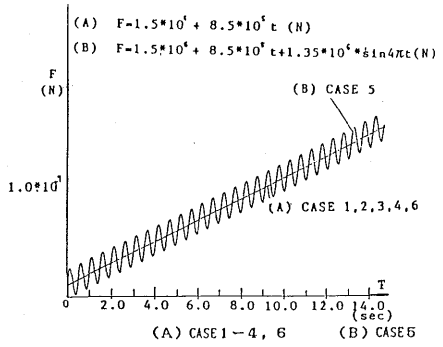

Fig. 4.1. Applied dynamic load to foundation.

4.2 Inferences

Figs. 4.6 and 4.7 show that the penetration depth in case 1 is larger than those in cases 2 and 3. There is no significant difference in the horizontal movement of particles in the three cases. In all cases, a significant movement of particles occurred within a region ap-

Table 4.1 Cases for numerical experiment of pile penetration

Case of numerical experiment	Friction coefficient		Width of foundations	Tensile force between particle	Type of load (in Fig. 4.1)	Radius of particle
	static μ_s	sliding μ_s				
Case 1	0.5	0.2	10 m	No	A	Uniform distribution
Case 2	0.5	0.2	30 m	No	A	Uniform distribution
Case 3	1.0	1.0	10 m	No	A	Uniform distribution
Case 4	0.5	0.2	10 m	No	A	Uniform distribution
Case 5	0.5	0.2	10 m	No	B	Uniform distribution
Case 6	0.5	0.2	10 m	No	A	Equal radius

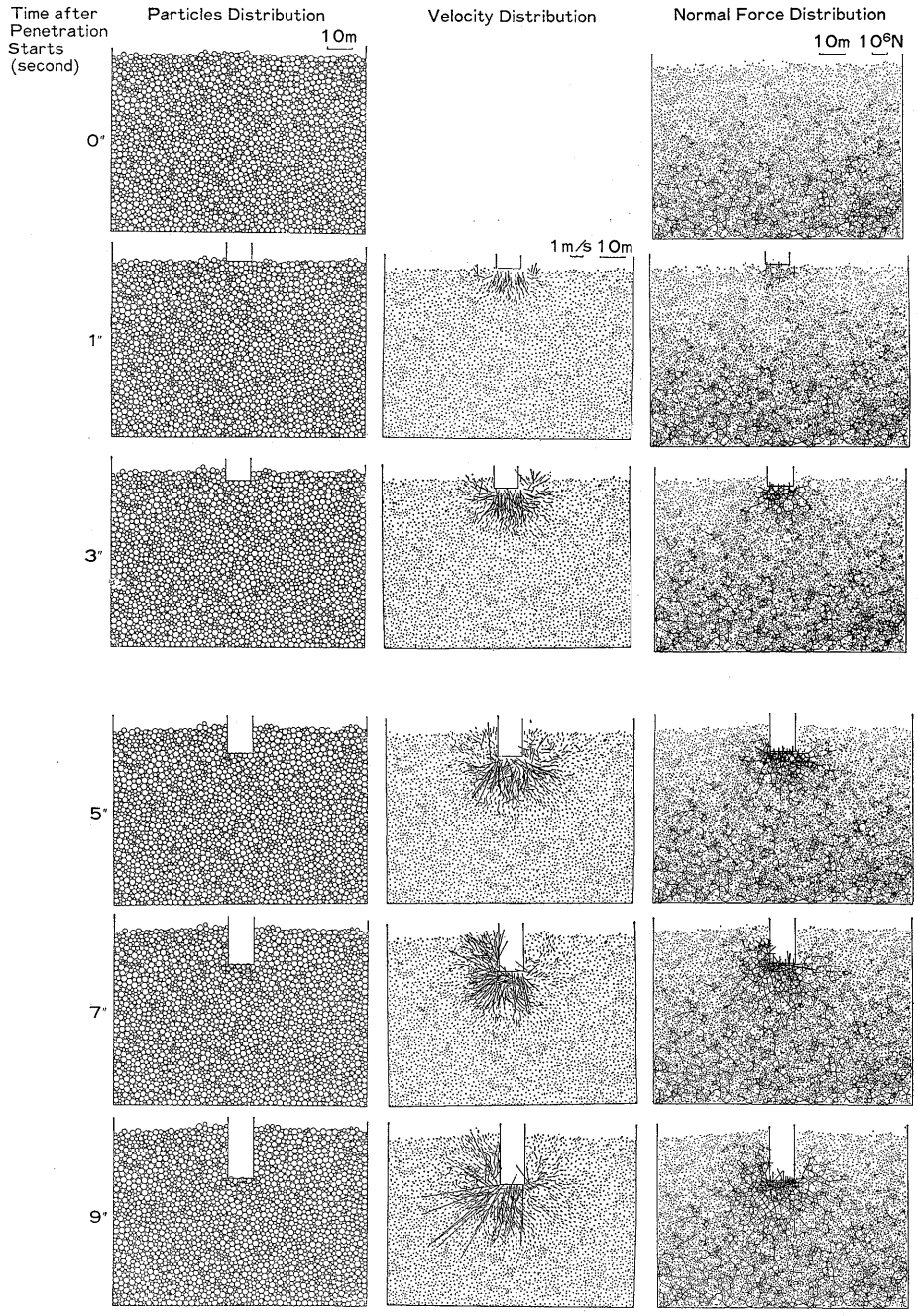

Fig. 4.2. Penetration of a pile into the ground. (to be continued on next page)

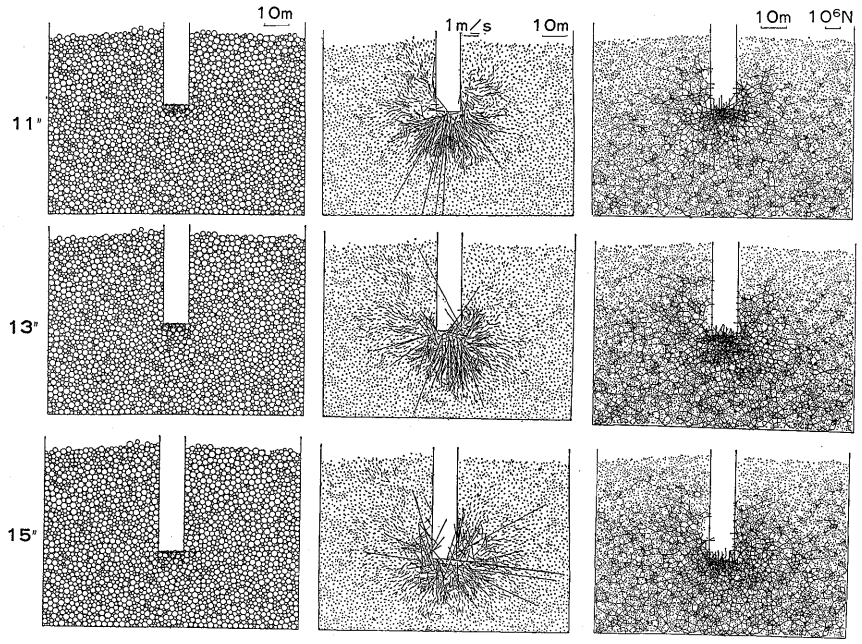

Fig. 4.2. Penetration of a pile into the ground.

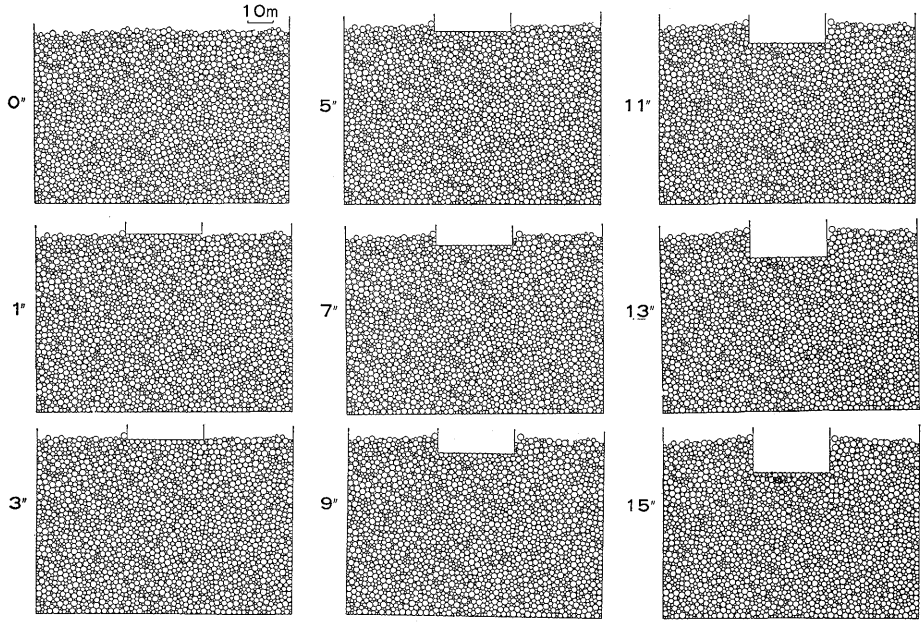

Fig. 4.3. Penetration of a direct structual foundation.

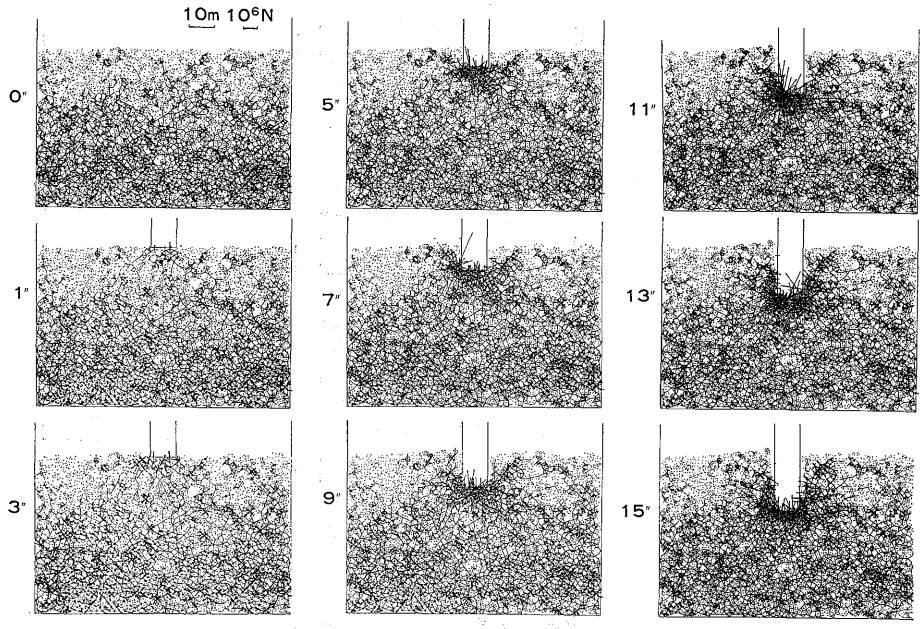

Fig. 4.4. Penetration of a pile into the ground in the case of particles having tensile strength. (Normal force distribution)

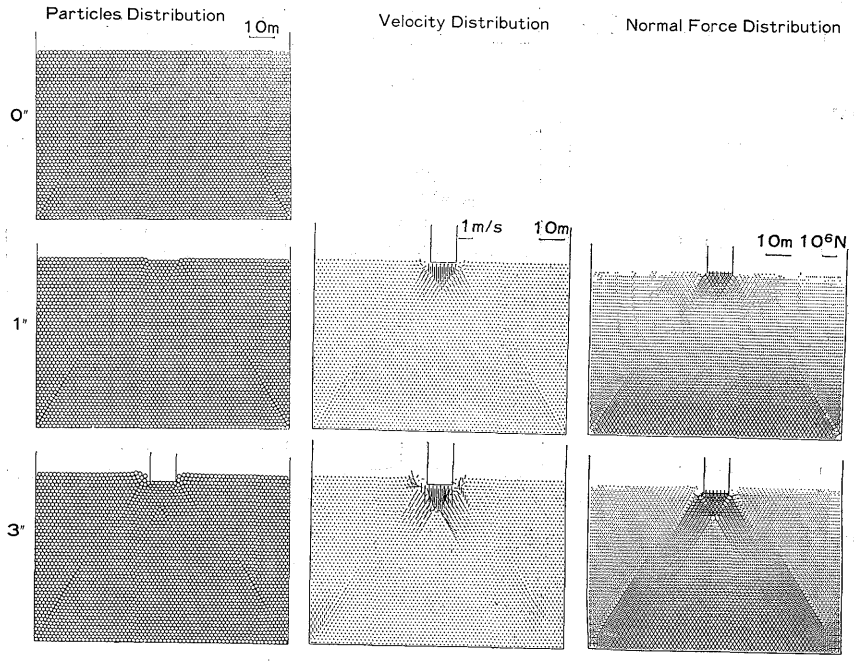

Fig. 4.5. Penetration of a pile into particles assembly with equal diameter. (to be continued on next page)

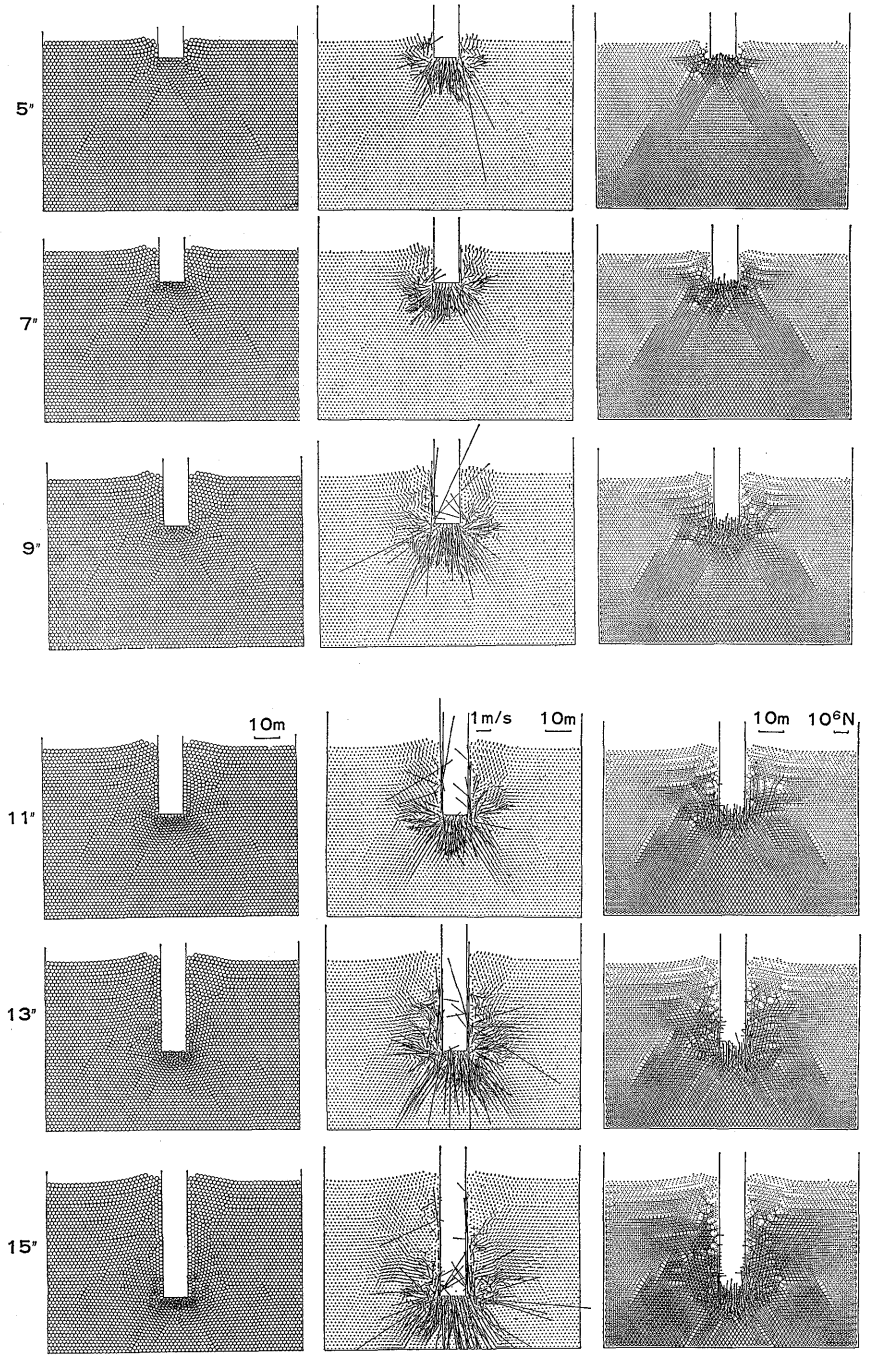

Fig. 4.5. Penetration of a pile into particles assembly with equal diameter.

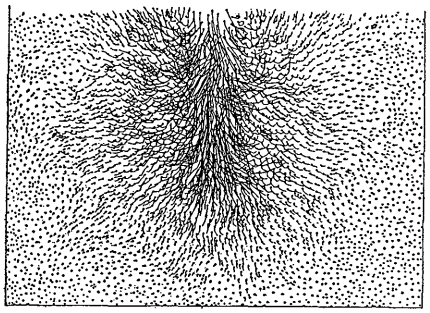

Fig. 4.6 (a) Loci of particles during penetration (case 1) (μ_S: 0.5, μ_D; 0.2, W: 10 m)

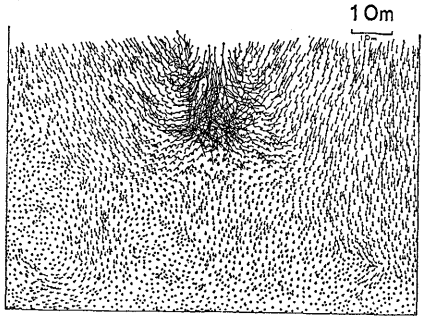

Fig. 4.6 (d) Loci of particles during penetration (case 4) (μ_S: 0.5, μ_D: 0.2, W: 10 m)

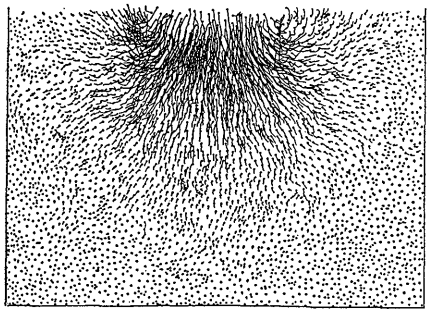

Fig. 4.6 (b) Case 2 (μ_S: 0.5, μ_D: 0.2, W: 30 m)

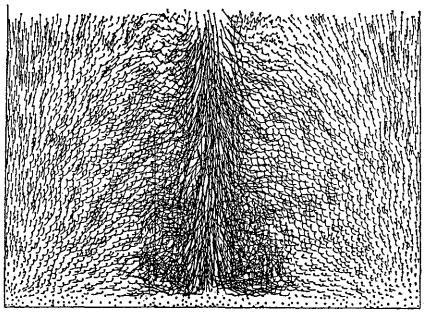

Fig. 4.6 (e) Case 5 (μ_S: 0.5, μ_D: 0.2, W: 10 m)

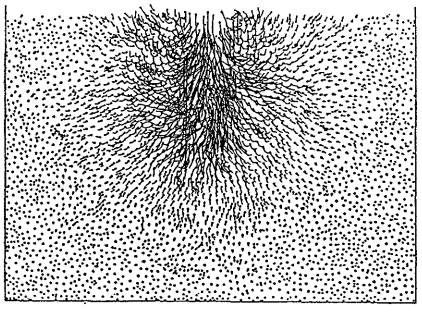

Fig. 4.6 (c) Case 3 (μ_S: 1.0, μ_D: 1.0, W: 10 m)

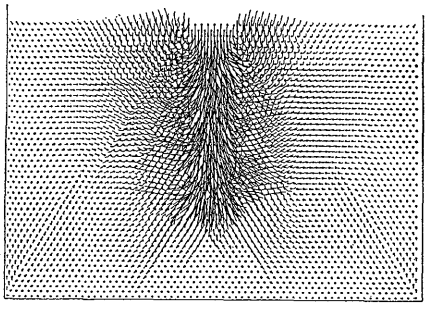

Fig. 4.6 (f) Case 6 (μ_S: 0.5, μ_D: 0.2, W: 10 m)

Fig. 4.6. Loci of particles during penetration (case 1–case 6). μ_S, static friction coefficient; μ_D, dynamic friction coefficient.

proximately 20 m around the pile on the ground surface. The results of case 4 (Fig. 4.4) show clearly that the penetrating force of the pile is transmitted widely in the horizontal direction. The tensile resistant forces between particles should also be considered. In case 5, the

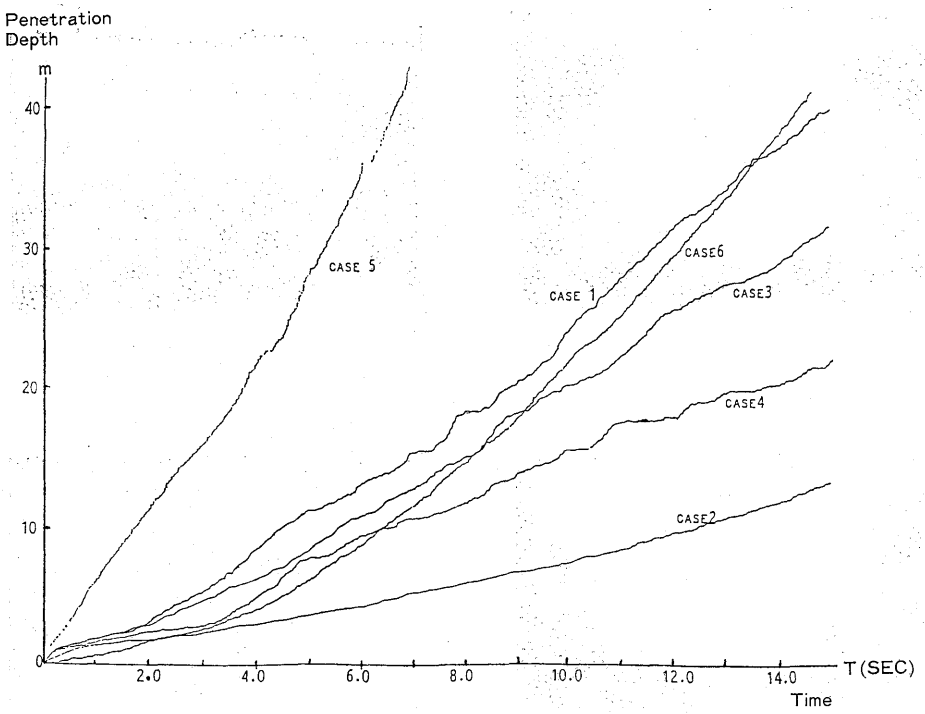

Fig. 4.7. Relation between panetration depth and time.

amount of subsidence and penetration of a pile is generally large.

It is qualitatively confirmed, according to the above mentioned results, that dynamic loadings cause a fairly wide ground subsidence. It serves also for the structure settlement even if the amplitude of dynamic loading is the same as that of the static loading.

In Figs. 4.2 to 4.5, it is characteristic that only some particles just below the pile have some motions with different velocities. This agrees with the natural phenomenon of a pile with a similar sharp end while penetrating the ground. It indicates that the slipping line appears right below the structure. In the last stage of penetration particles have moved in a direction completely different from that in the first stage (Fig. 4.6). Fig. 4.4 shows that the tensile forces between particles spread in a horizontal direction during penetration. These tensile forces disappear either near the ground surface or the pile. Fig. 4.4 also indicates that the tensile forces between particles act only in the horizontal direction while the compressive forces act only in the vertical direction, i.e. the deeper the place, the greater the compressive forces. The tensile forces do not have such a tendency but they occur locally.

In case 6 a plastic domain appears clearly in a small range of

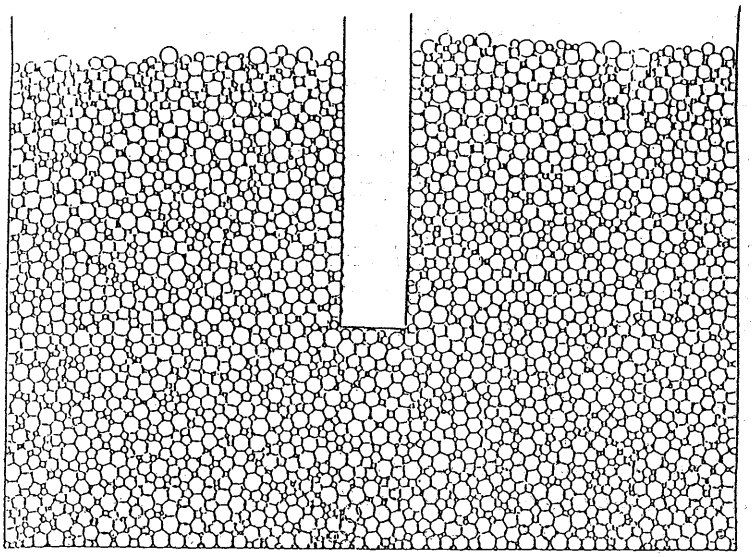

Fig. 5.1 (a) Assembly model for pile foundation (2 Hz, pile) (0.5 Hz, pile).

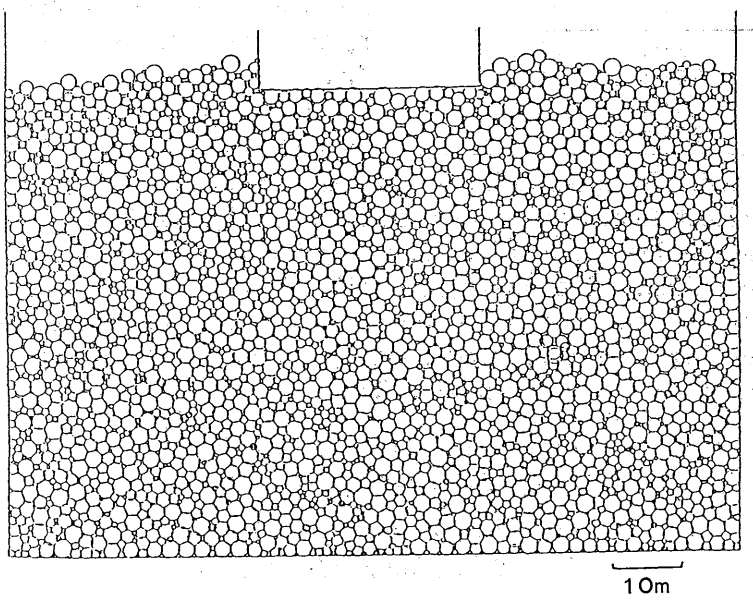

Fig. 5.1 (b) Assembly model for direct foundation (2 Hz, direct) (0.5 Hz, direct).

penetration.

Generally, soil response differs according to the site conditions and the ways of loading. For example, particles of the ground surface close to the pile float up sometimes in spite of the fact that most of them go down with the pile.

5. Dynamic Nonlinear Response of Structural Foundations

The nonlinear properties of a structure and its surrounding soil should be taken into consideration while analyzing the response of that structure under the loading conditions of earthquakes, winds, etc. The movements of individual soil particles cannot be cleared by means of the conventional continuum mechanics. The granular assembly simulation might be suitable for individual particles behavior analysis.

The behavior of a pile and a direct foundation under different horizontal dynamic loadings were analyzed also using the previous model.

5.1 Model

The analysis was carried out for the four cases mentioned in Table 5.1. Dynamic loads were applied to a pile buried deeply in the ground as shown in Fig. 5.1 (a) (cases 1-A and 1-B). The model was simulated by releasing the concentrated stress right under the pile obtained by the penetration simulation in Fig. 4.2.

Table 5.1 Cases for dynamic response of foundation

Case	Frequency of external force	Type of foundation
1-A	2 Hz	Pile
1-B	0.5 Hz	Pile
2-A	2 Hz	Direct
2-B	0.5 Hz	Direct

In this model, the pile is 9.0 m wide, 100 m long and 60 m deep in the ground. In cases 2-A and 2-B, the dynamic loading was applied to the direct foundation shown in Fig. 5.1 (b). This assembly model was also obtained from Fig. 4.3 using the same procedure as in the pile foundation. The direct foundation is 30 m wide, 30 m long and five meters deep. The horizontal dynamic loads were determined using the following equations. These loads were applied to the above stated pile and direct foundations (Fig. 5.2).

$$\text{Case 1-A, } F=5.0\times10^{3}\times t\sin\pi t \tag{5.1.a}$$

$$\text{Case 1-B, } F=5.0\times10^{3}\times t\sin 4\pi t \tag{5.1.b}$$

$$\text{Case 2-A, } F=5.0\times10^{4}\times t\sin\pi t \tag{5.1.c}$$

$$\text{Case 2-B, } F=5.0\times10^{4}\times t\sin 4\pi t \tag{5.1.d}$$

where the unit of F is N.

Loading positions are at the pile's top and at a point five meters below the top of the direct foundation. Other assumptions were made so that both types of foundation were permitted to rotate around their bases' center. In other words, when ($X1$, $Z1$) is the coordinate of the foundation base center, the inclined angle θ of the foundation (rad) is positive in the clockwise direction and the width is $B(m)$. The fol-

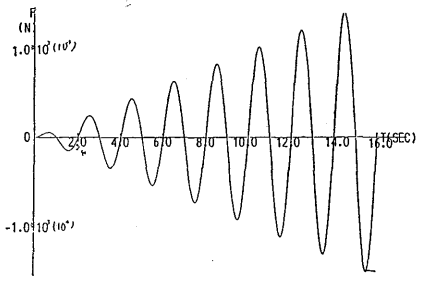

(a)

Fig. 5.2 (a) Applied dynamic force with frequency of 0.5 Hz, (0.5 Hz, pile) (0.5 Hz, direct).

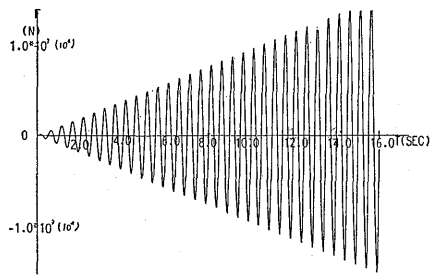

(b)

Fig. 5.2 (b) Applied dynamic force with frequency of 2 Hz, (2 Hz, pile) (2 Hz, direct).

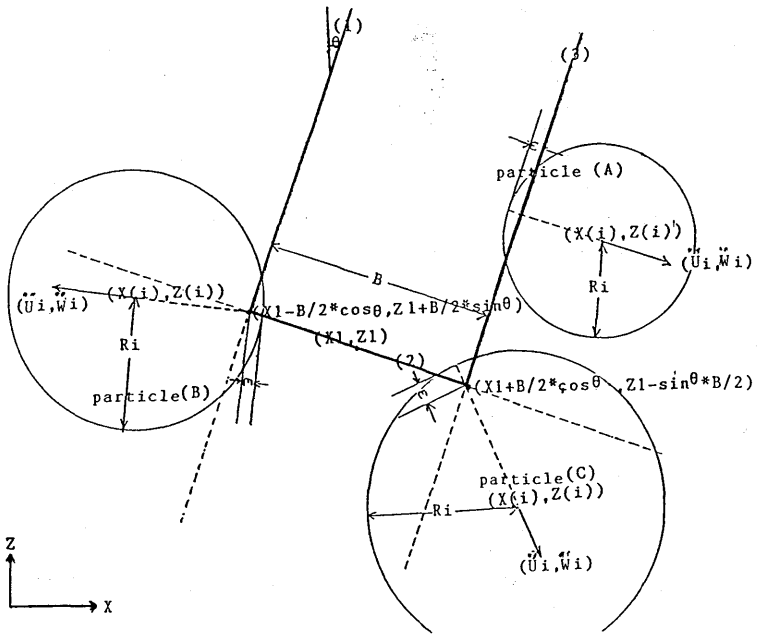

Fig. 5.3. Illustration for particles and foundation.

lowing equations of the straight lines (1), (2), (3) express the foundations

(1) where $\theta \neq 0, 0, \quad Z=aX+b$ (5.2.a)

$$\left(a=\tan\left(\frac{\pi}{2}-\theta\right), \quad b=Z1+\mathrm{B}\sin\frac{\theta}{2}+\tan\left(\frac{\pi}{2}-\theta\right)\cdot\left(\frac{B}{2}\cos\theta-X1\right)\right)$$

(2) where $\theta=0.0, \quad X=X1-B/2, \quad Z=aX+b$ (5.2.b)

$$(a=-\tan\theta, \quad b=Z1+\tan\theta\cdot X1)$$

(3) where $\theta \neq 0.0$, $Z=aX+b$ (5.2.c)

$$\left(a=\tan\left(\frac{\pi}{2}-\theta\right),\quad b=Z1-B\sin\frac{\theta}{2}-\tan\left(\frac{\pi}{2}-\theta\right)\cdot\left(\frac{B}{2}\cos\theta+X1\right)\right)$$

Adding the following conditions,

(1) $$Z>Z1+\frac{B}{2}\sin\theta \tag{5.3.a}$$

(2) $$X1-\frac{B}{2}\cos < X < X1+\frac{B}{2}\cos\theta \tag{5.3.b}$$

(3) $$Z>Z1-\frac{B}{2}\sin\theta \tag{5.3.c}$$

A particle with a radius r_i when located at (X_i, Z_i) makes a contact with the above mentioned lines as follows:

$$\varepsilon=r_i-|Z_i-aX_i-b|/\sqrt{1+a^2}>0.0,\ (\theta\neq 0.0) \tag{5.4.a}$$

$$\varepsilon=X_i+r_i-\left(X1-\frac{B}{2}\right)>0.0,\ \text{(when (5.3.a), } \theta=0.0) \tag{5.4.b}$$

$$\varepsilon=X1+\frac{B}{2}-X_i+r_i>0.0,\ \text{(when (5.3.c), } \theta=0.0) \tag{5.4.c}$$

where the projection point (X_c, Z_c) of the center of each particle at each line should satisfy the following equations:

$$X_c=a/\sqrt{1+a^2}\cdot(X_i/a+Z_i-b) \tag{5.5.a}$$

$$Z_c=a/\sqrt{1+a^2}\cdot(X_i+aZ_i+b/a) \tag{5.5.b}$$

The particle's acceleration $(\ddot{u}, \ddot{w})$ is induced by the foundation as,

$$\ddot{u}=\varepsilon\cdot K_n\cdot(X_i-X_c)/\sqrt{(X_i-X_c)^2+(Z_i-Z_c)^2} \tag{5.6.a}$$

$$\ddot{w}=\varepsilon\cdot K_n\cdot(Z_i-Z_c)/\sqrt{(X_i-X_c)^2+(Z_i-Z_c)^2} \tag{5.6.b}$$

The moment M_F exerts by this particle on the foundation can be expressed as follows:

(1) $$M_{F_1}=\varepsilon\cdot K_n\cdot\left(Z_c-Z1-\frac{B}{2}\sin\theta\right)\cdot\sec\theta \tag{5.7.a}$$

(2) $$M_{F_2}=\varepsilon\cdot K_n\cdot(X1-X_c)\cdot\sec\theta \tag{5.7.b}$$

(3) $$M_{F_3}=\varepsilon\cdot K_n\cdot\left(Z1-Z_c-\frac{B}{2}\sin\theta\right)\cdot\sec\theta \tag{5.7.c}$$

(K_n is a spring coefficient)

The analysis of the rotational response of foundations was carried out using the sum of particles moment obtained by the previous equ-

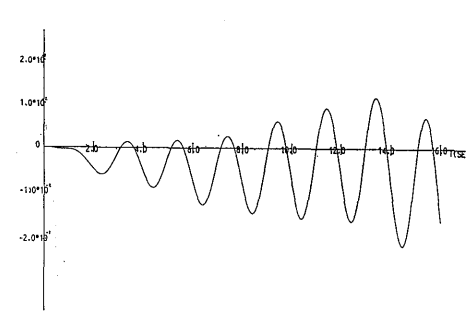

Fig. 5.4 (a) Angular response of a pile foundation (0.5 Hz, pile).

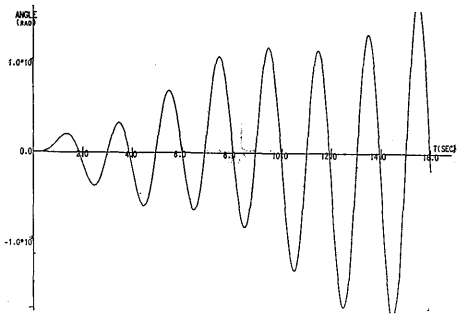

Fig. 5.4 (c) Angular response of a direct foundation (0.5 Hz, direct).

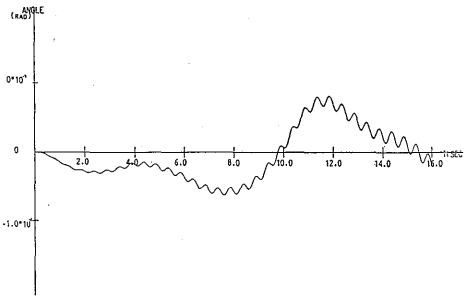

Fig. 5.4 (b) Angular response of a pile foundation (2 Hz, pile).

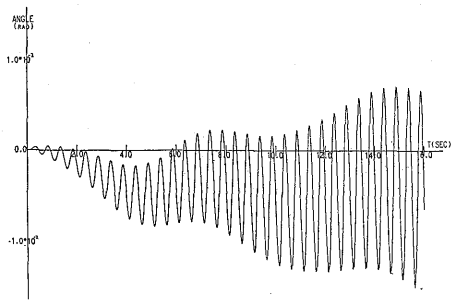

Fig. 5.4 (d) Angular response of a direct foundation (2 Hz, direct).

ations, the moment of the dead weight of the foundation itself and the moment of the external forces shown in Fig. 5.2.

5.2 Results of Simulation

The simulation results of time history of the angle and moment of a foundation are given in Figs. 5.4 to 5.5. In Fig. 5.4, a small vibration response up to 2.0×10^{-2} rad shows nonlinear properties. A foundation of 10 m depth will be displaced up to 10 cm depending on the force. Fig. 5.5 shows large vibrations of a foundation when inclined up to 0.4 rad corresponding to the soil behavior in plastic domain. Fig. 5.6 shows hysteresis loops (the relationship between the moment to the foundation and the angular response) utilizing data of Fig. 5.5. Fig. 5.7 indicates the loci of particles related to cases 1-A and 1-B. Twelve particles have been chosen as shown in Fig. 5.7 (a), the locus of each particle has been detected. The numerals in brackets (right lower part of each figure) indicate the horizontal and vertical distances to the chosen particle's center measured from the lower left corner of the original model. Units are in meters.

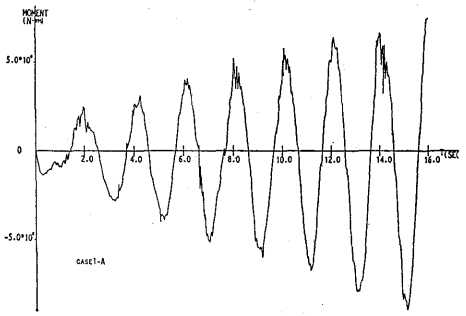

Fig. 5.5 (a) Moment response of a pile (0.5 Hz, pile).

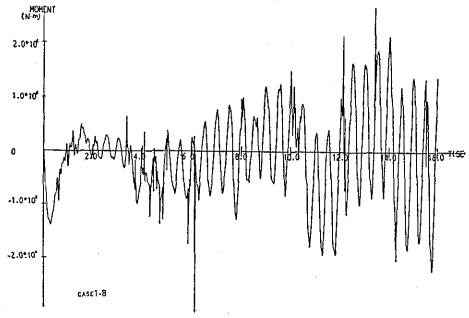

Fig. 5.5 (b) Moment response of a pile (2 Hz, pile).

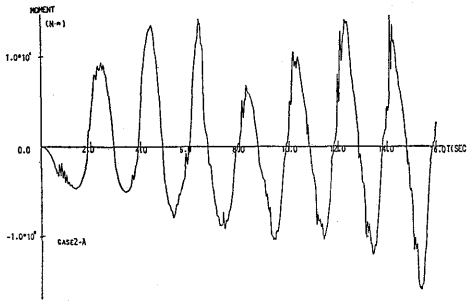

Fig. 5.5 (c) Moment response of a direct foundation (0.5 Hz, direct).

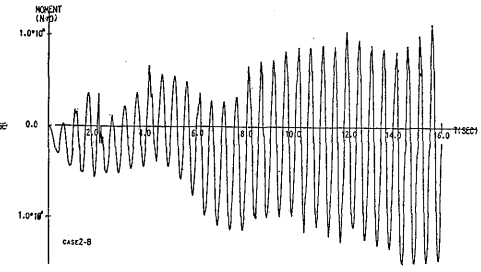

Fig. 5.5 (d) Moment response of a direct foundation (2 Hz, direct).

Fig. 5.8 shows the location, velocity and normal force of particles corresponding to approximately 0.1, 0.2, 0.3, and 0.4 rad after long dynamic excitation. Fig. 5.9 shows the same as Fig. 5.8 for the direct foundation.

5.3 Inferences

Fig. 5.7 shows that the higher the frequency of external force, the more complicated the motion of each particle. Such motion resembles the motion of same external force's frequency together with a lower frequency motion. Individual particles mostly subside during the vibration, but they float up in some cases. The amplitude of the angular response of the foundation is greater when the frequency of external force is 0.5 Hz than when 2 Hz even if it has the same amplitude. The external force of lower frequency gives more energy to the foundation in one cycle of the vibration which might cause this phenomenon. In Fig. 5.6 (a to d), a linear relationship is clearly defined between the angular response of the foundation and the external force when the later is weak. When the external force increases

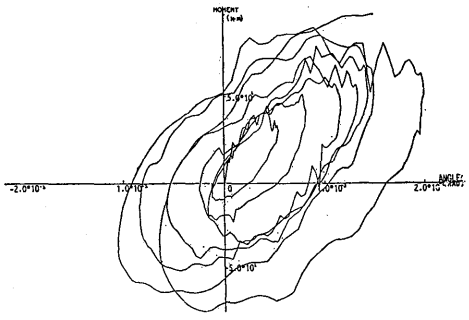

Fig. 5.6 (a) Relation between moment and response angle of a pile (0.5 Hz, pile).

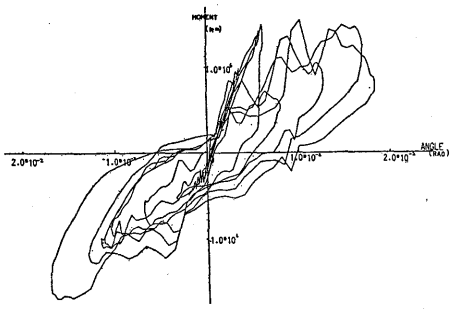

Fig. 5.6 (c) Relation between moment and response angle of a direct foundation (0.5 Hz, direct).

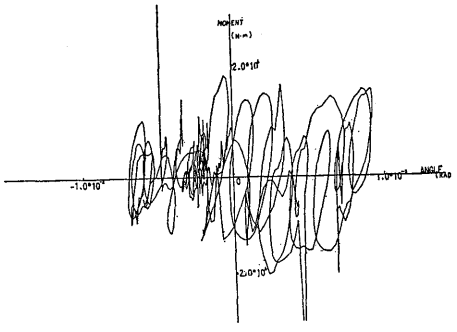

Fig. 5.6 (b) Relation between moment and response angle of a pile (2 Hz, pile).

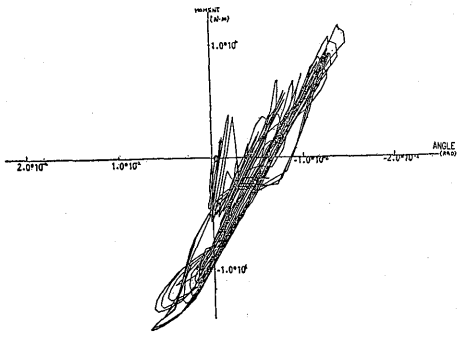

Fig. 5.6 (d) Relation between moment and response angle of a direct foundation (2 Hz, direct).

the area of the hysteresis loop gets larger and the spring constant becomes smaller. Then, nonlinear relationships are defined. This trend is especially well seen in the case of the direct foundation.

The relationship of Fig. 5.6 (b) is quite different from the others. This might be caused by the large deviation of the angular response's neutral axis due to large plastic deformation.

In the direct foundation the spring softens in the relationships between the angular response and the high frequency external but the area of the hysteresis loop remains almost zero for large amplitudes of the external force.

The subsidence due to vibration occurred as a whole in Fig. 5.7. The subsidence is larger in places close to the foundation and to the ground surface. The results of the direct foundation show that an overturn collapse of a direct foundation under a strong earthquake motion is caused due to the continuous increase of the angular response in one direction. At a critical angle of inclination, the moment of the

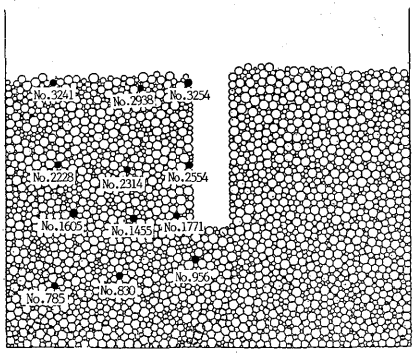

Fig. 5.7 (a) Position of sample particles.

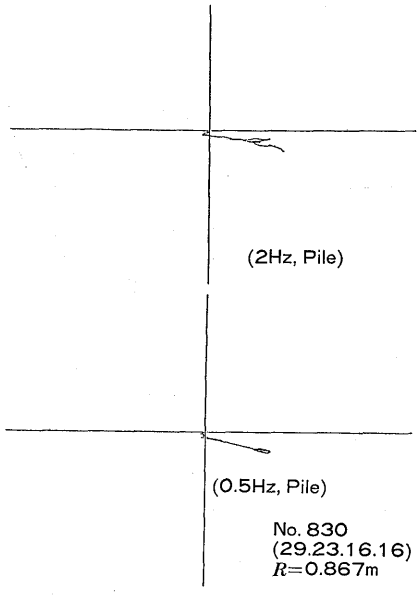

Fig. 5.7 (b) Loci of sample particle (2 Hz, pile) (0.5 Hz, pile).

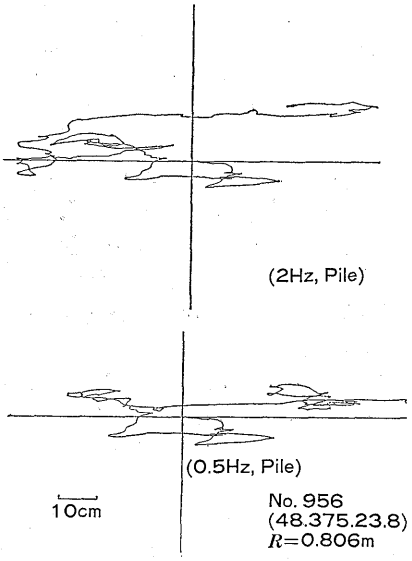

Fig. 5.7 (c) Loci of sample particle (2 Hz, pile) (0.5 Hz, pile).

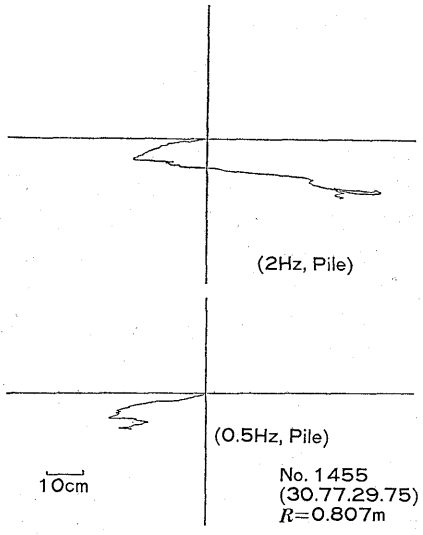

Fig. 5.7 (d) Loci of sample particle (2 Hz, pile) (0.5 Hz, pile).

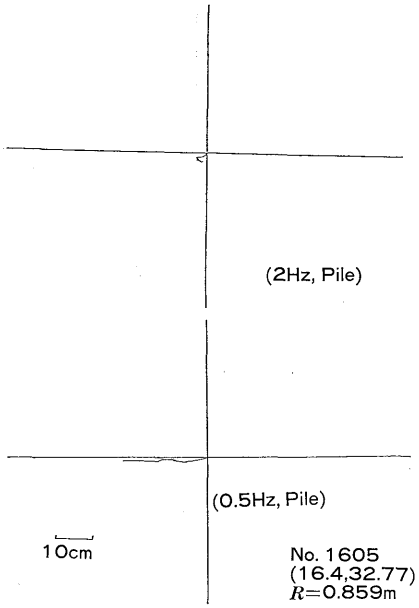

Fig. 5.7 (e) Loci of sample particle (2 Hz, pile) (0.5 Hz, pile).

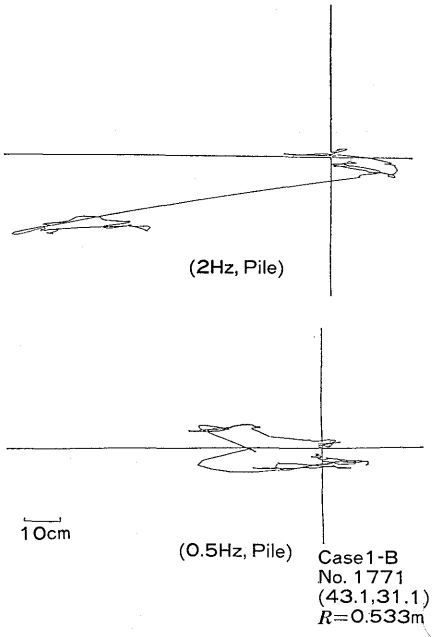

Fig. 5.7 (f) Loci of sample particle (2 Hz, pile) (0.5 Hz, pile).

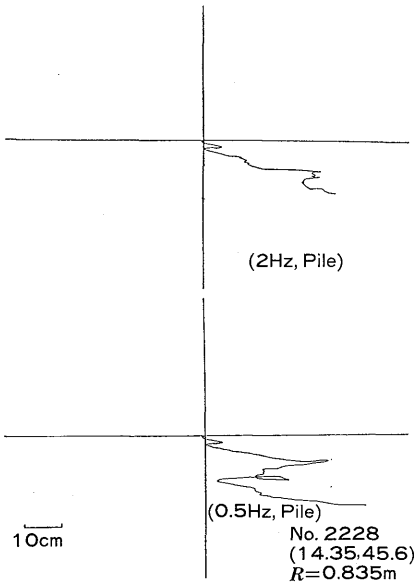

Fig. 5.7 (g) Loci of sample particle (2 Hz, pile) (0.5 Hz, pile).

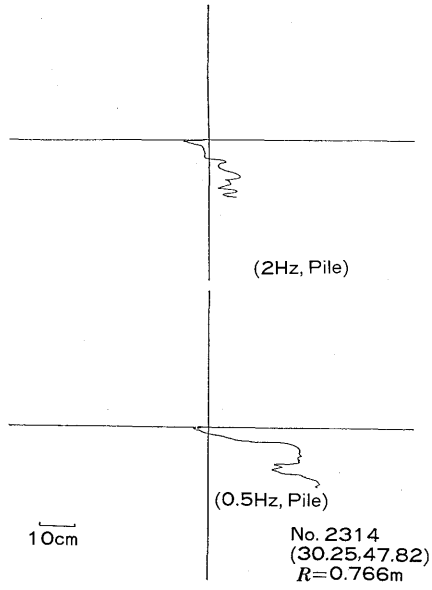

Fig. 5.7 (h) Loci of sample particle (2 Hz, pile) (0.5 Hz, pile).

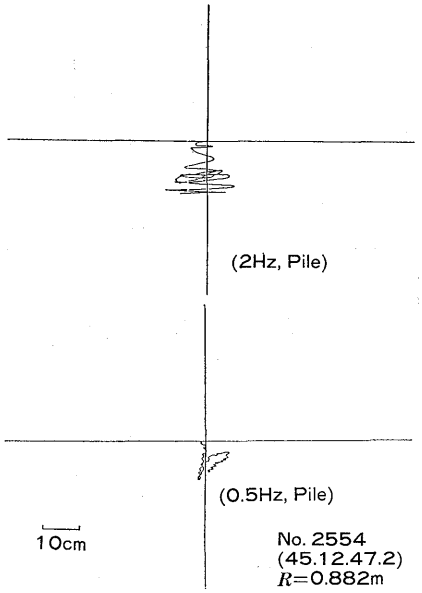

Fig. 5.7 (i) Loci of sample particle (2 Hz, pile) (0.5 Hz, pile).

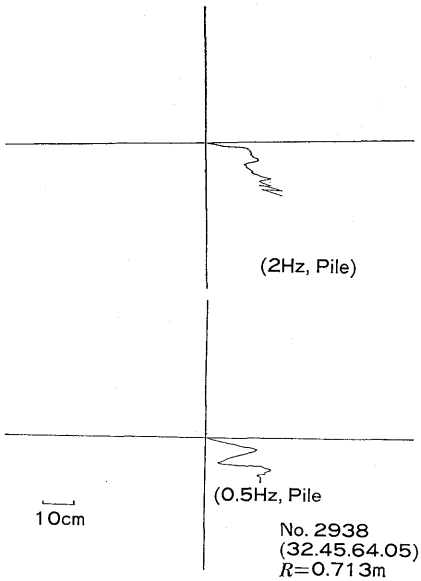

Fig. 5.7 (j) Loci of sample particle (2 Hz, pile) (0.5 Hz, pile).

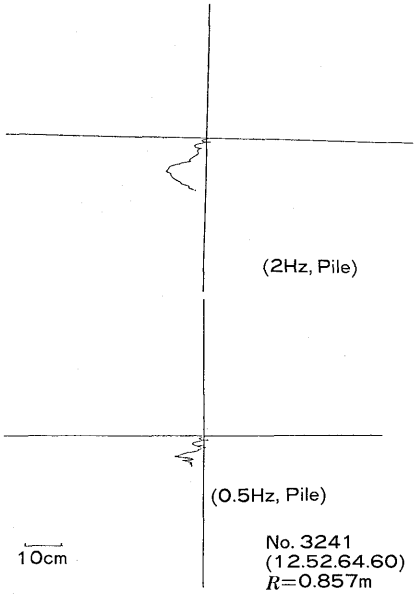

Fig. 5.7 (k) Loci of sample particle (2 Hz, pile) (0.5 Hz, pile).

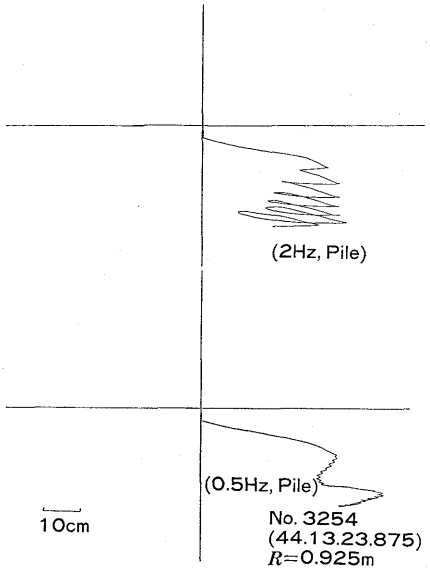

Fig. 5.7 (l) Loci of sample particle (2 Hz, pile) (0.5 Hz, pile).

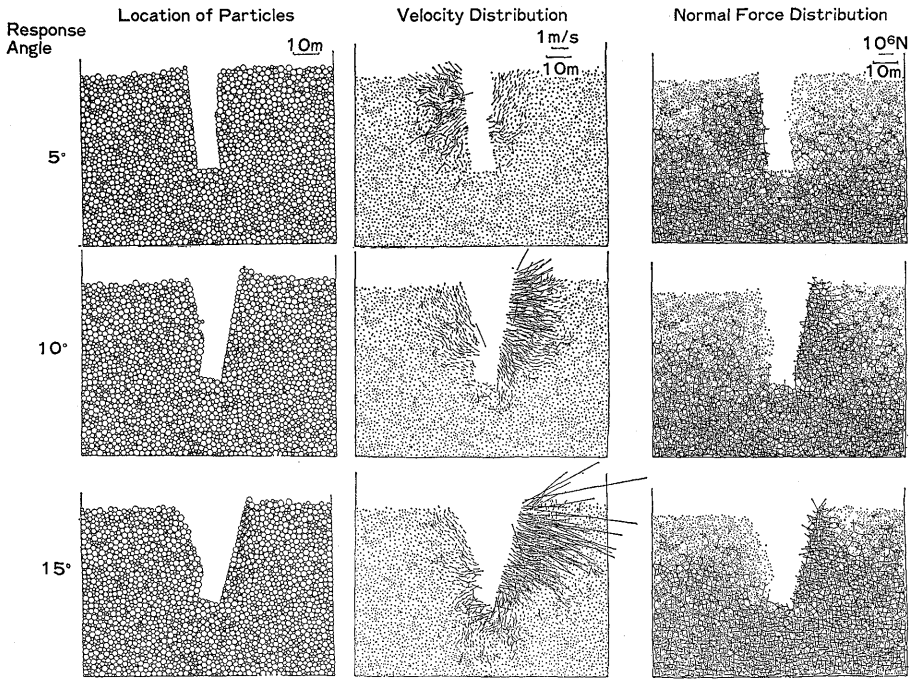

Fig. 5.8. Angular response of a pile foundation.

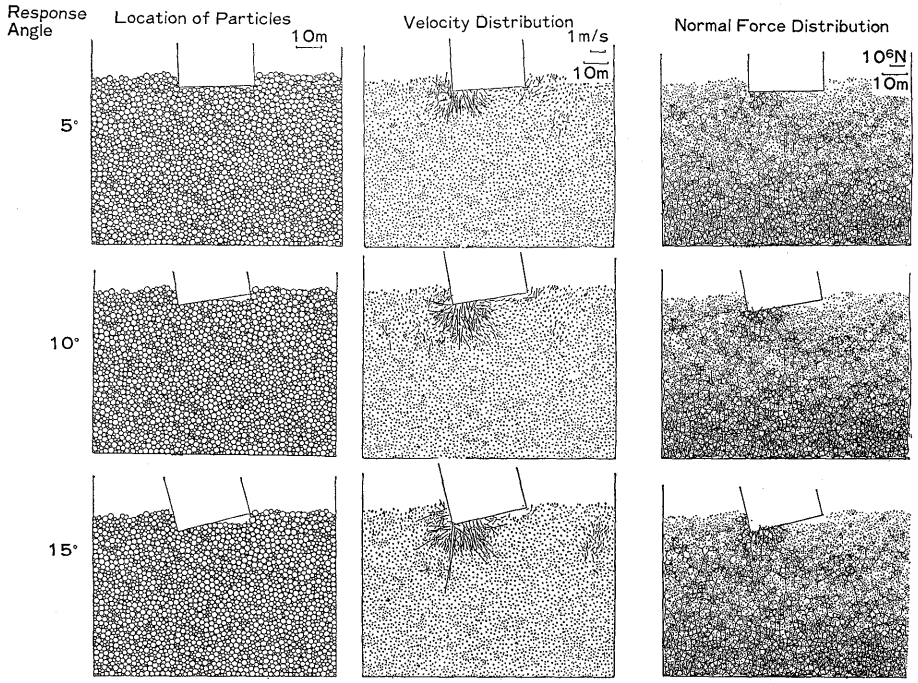

Fig. 5.9. Angular response of a direct foundation (to be continued on next page)

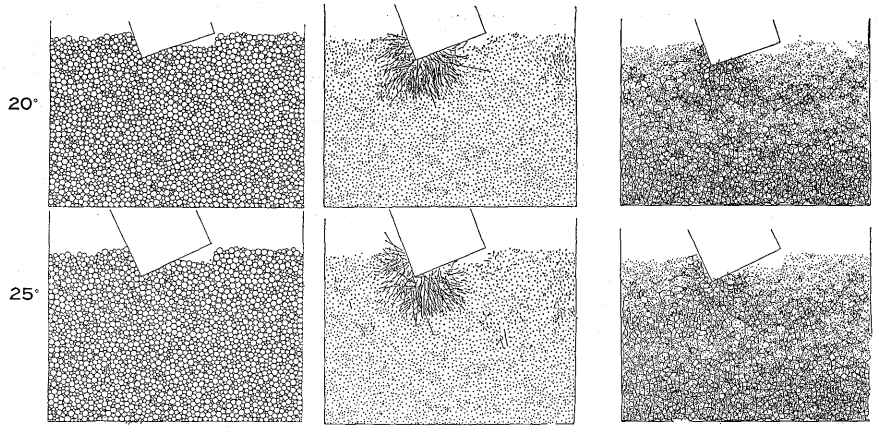

Fig. 5.9. Angular response of a direct foundation. (continued)

foundation's weight acts to accelerate the overturning. This is the reverse direction of the restoring force.

The results of the above mentioned simulation led to the following;

1. The nonlinear relationship between the external force and the response of the foundation, obtained by field tests, was confirmed by this simulation. It is significant that these nonlinear relationships were derived only from particle coefficients such as the coefficient of friction, the elastic spring constant, etc.

2. The overturning process of direct foundation was analyzed qualitatively. The foundation structure stops vibrating back and forth as the deadweight of the structure serves to increase the inclination angle. When the vibration amplitude becomes larger to a certain extent, the structure overturns on one side.

6. Analyses of Dynamic Earth Pressure of Loose Ground under Dynamic Excitations

The dynamic earth pressure on retaining walls during earthquakes is a critical object. It has been faced by several difficulties. First of all, it is difficult to satisfy the law of similitude completely in laboratory experiments. It is difficult to generate the strong ground motion that causes the damage of structures during field tests. It is also diffiult to grasp additional earth pressure, caused by the subsidence of the ground soil, utilizing the conventional continuum mechanics.

These problems have been solved using the simulation of the granular assembly. A simulation analysis of the dynamic earth pressure on the retaining wall was performed for various frequencies, acceleration amplitudes of the dynamic loadings and friction coefficients

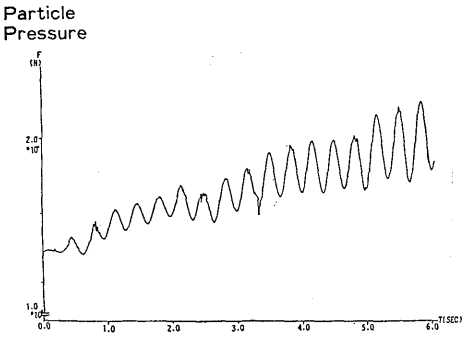

Fig. 6.1 (a) Time history of sum of particle pressure on the wall under horizontal vibration (400 gal, 3.6 Hz, μ_S: 0.5, μ_D: 0.2)

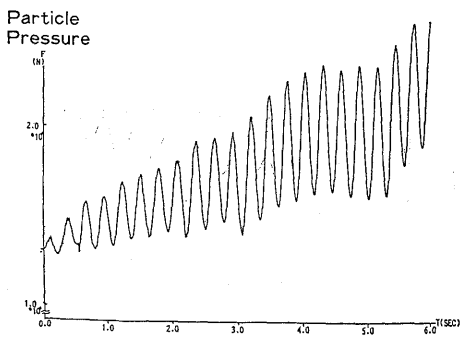

Fig. 6.1 (b) (800 gal, 3.6 Hz, μ_S: 0.5, μ_D: 0.2)

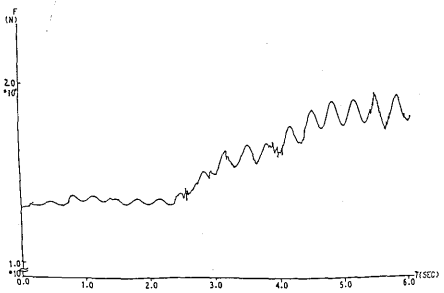

Fig. 6.1 (c) (200 gal, 3.6 Hz, μ_S: 0.5, μ_D: 0.2)

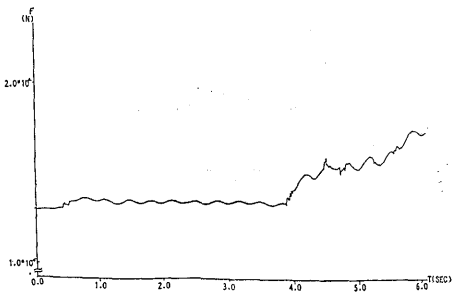

Fig. 6.1 (d) (100 gal, 3.6 Hz, μ_S: 0.5, μ_D: 0.2)

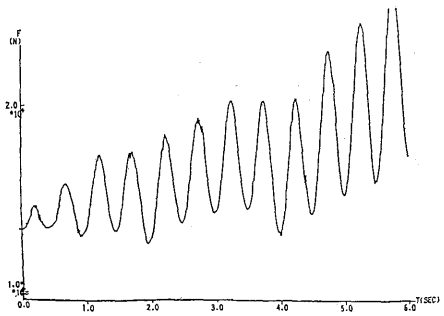

Fig. 6.1 (e) (800 gal, 2.0 Hz, μ_S: 0.5, μ_D: 0.2)

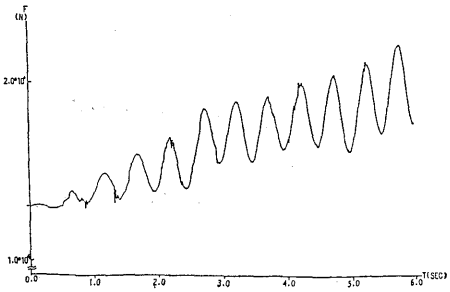

Fig. 6.1 (f) (400 gal, 2.0 Hz, μ_S: 0.5, μ_D: 0.2)

of soil particles.

6.1 Particle Model for the Simulation

The same number of particles used in the previous models was used in this model. The model size was changed to be eight meters

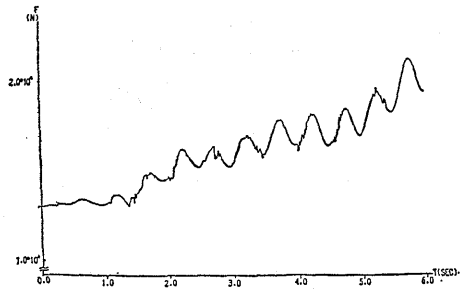

Fig. 6.1 (g) (200 gal, 2.0 Hz, μ_S: 0.5, μ_D: 0.2)

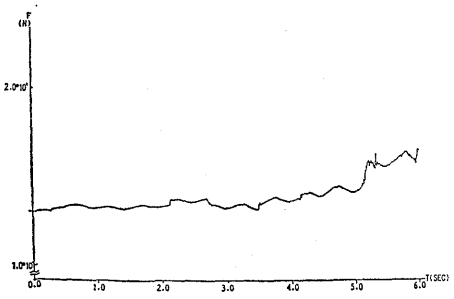

Fig. 6.1 (h) (100 gal, 2.0 Hz, μ_S: 0.5, μ_D: 0.2)

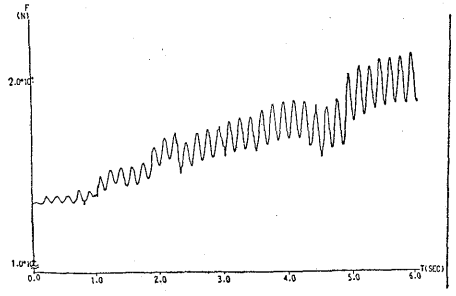

Fig. 6.1 (i) (400 gal, 6.0 Hz, μ_S: 0.5, μ_D: 0.2)

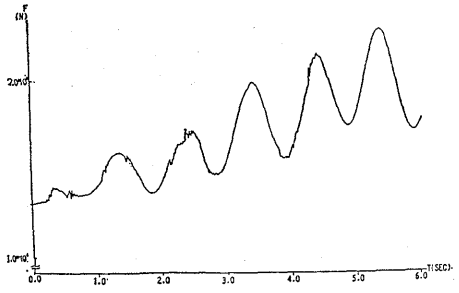

Fig. 6.1 (j) (400 gal, 1.0 Hz, μ_S: 0.5, μ_D: 0.2)

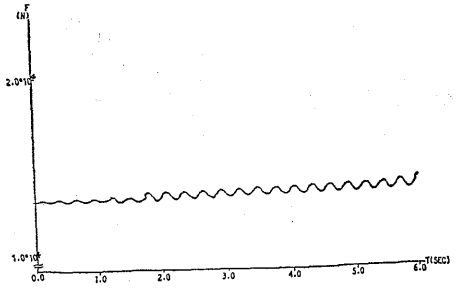

Fig. 6.1 (k) (400 gal, 3.6 Hz, μ_S: 1.0, μ_D: 0.5)

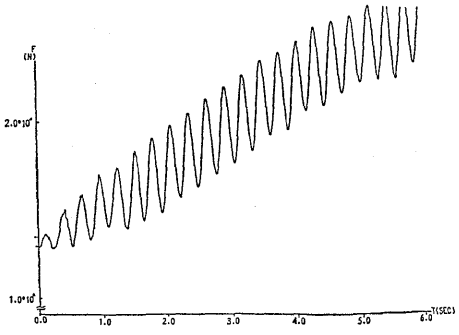

Fig. 6.1 (l) (400 gal, 3.6 Hz, μ_S: 0.2, μ_D: 0.2)

long and 5.6 m deep. External forces proportional to a sine wave acceleration multiplied by the mass of an individual particle were applied to each particle. The various cases of simulations are shown in Table 6.1.

6.2 Calculation Results

In order to study the earth pressure during a comparatively short

Table 6.1 Twelve cases of horizontal vibration

Case	Vibration		Particle coefficient	
	Acceralation (gal)	Frequency (Hz)	Friction (Static)	Friction (Dynamic)
1	400	3.6	0.5	0.2
2	800	3.6	0.5	0.2
3	200	3.6	0.5	0.2
4	100	3.6	0.5	0.2
5	800	2.0	0.5	0.2
6	400	2.0	0.5	0.2
7	200	2.0	0.5	0.5
8	100	2.0	0.5	0.2
9	400	6.0	0.5	0.2
10	400	1.0	0.5	0.2
11	400	3.6	1.0	0.5
12	400	3.6	0.2	0.2

time earthquake microscopically, the time history for six seconds vibration's duration of the total particle pressures acting on the right side wall is given in Fig. 6.1. Fig. 6.2 shows the distribution of the normal forces acting on the wall. Six cases of total particle pressures including the pressure of each particle on the wall, under sinusoidal excitation for 25 seconds are shown in Figs. 6.1 to 6.4. Figs. 6.5 and 6.6 show individual particle settlement every four seconds under 25 seconds of sinusoidal excitation (Case 2). The numerals in the upper part of Fig. 6.6 indicate the horizontal and vertical distance measured from the left bottom corner of the model. The small circles resemble the central location of particles. Fig. 6.7 shows the normal force distribution every four seconds and Fig. 6.8 shows the velocity distribution of particles during the vibration. Fig. 6.9 shows how particles subside during the vibration.

6.3 Inferences

Fig. 6.1 demonstrates that the DC component of the total particle forces acting on the wall is almost constant, at least for a while after the shaking starts and the larger the friction coefficient of particles, the longer the DC component. Therefore, the increase of the DC component after a short period of constant value seems to be due to the settlement and compaction of particles.

The relationship between frequencies of vibration and earth pressure can be explained by the following:

A larger increase of earth pressure and a greater force of particles are obtained by shaking with lower frequencies. This gives a similar trend of the results in Section 5. In case of a high frequency of

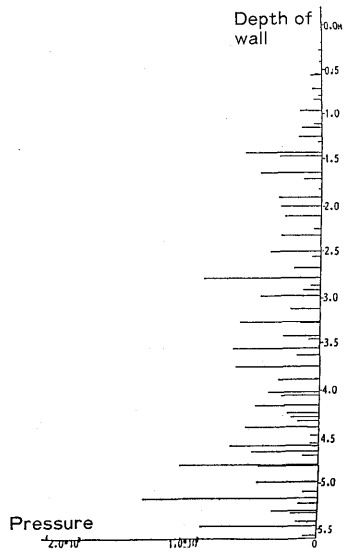

Fig. 6.2 (a) Particles pressure on the wall (before vibration)

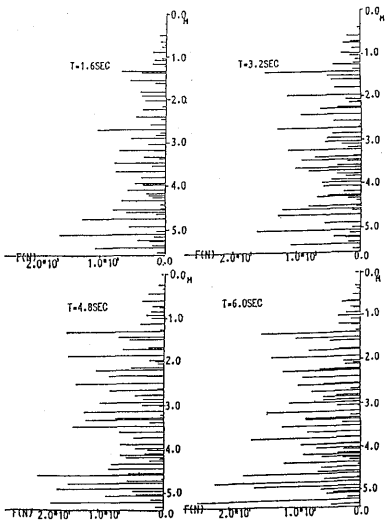

Fig. 6.2 (b) Particles pressure on the wall (400 gal, 3.6 Hz, μ_S: 0.5, μ_D: 0.2)

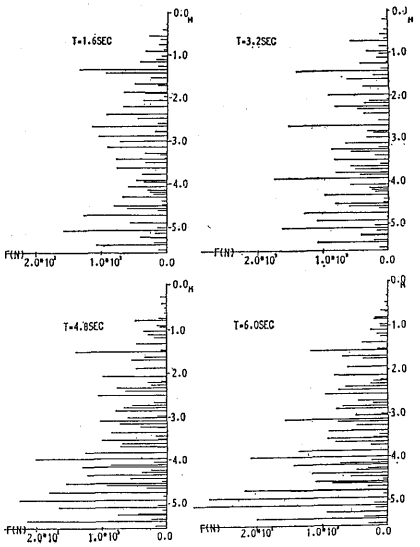

Fig. 6.2 (c) Particles pressure on the wall (800 gal, 3.6 Hz, μ_S: 0.5, μ_D: 0.2)

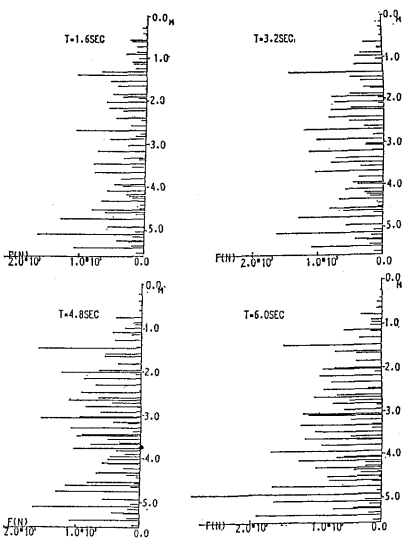

Fig. 6.2 (d) Particles pressure on the wall (200 gal, 3.6 Hz, μ_S: 0.5, μ_D: 0.2)

shaking, the subsidence compaction of particles starts late and the increase of DC component of the earth pressure also starts later. The relationships between the friction coefficient and earth pressure by

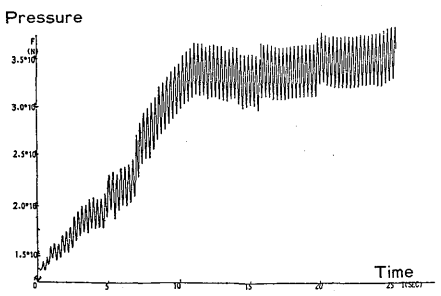

Fig. 6.3 (a) Time history of the amount of pressure on the wall under horizontal vibration. (800 gal, 3.6 Hz, μ_S: 0.5, μ_D: 0.2)

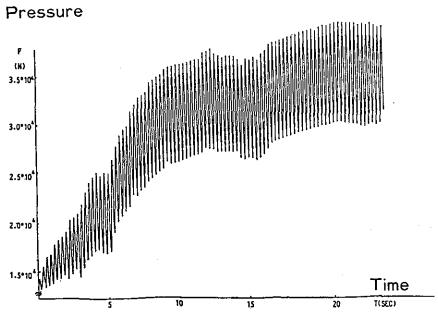

Fig. 6.3 (b) Time history of the amount of pressure on the wall under horizontal vibration (800 gal, 3.6 Hz, μ_S: 0.5, μ_D: 0.2)

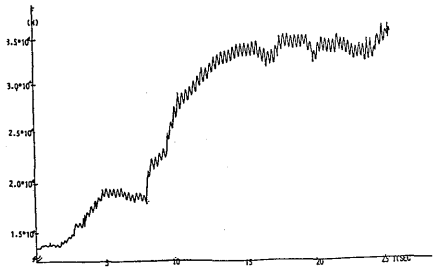

Fig. 6.3 (c) Time history of the amount of pressure on the wall under horizontal vibration. (100 gal, 3.6 Hz, μ_S: 0.5, μ_D: 0.2)

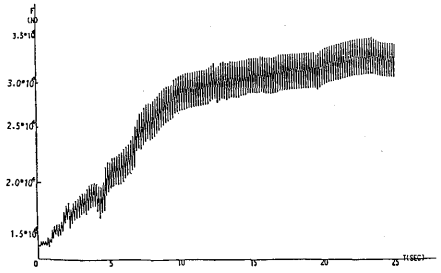

Fig. 6.3 (d) Time history of the amount of pressure on the wall under horizontal vibration. (400 gal, 6.0 Hz, μ_S: 0.5, μ_D: 0.2)

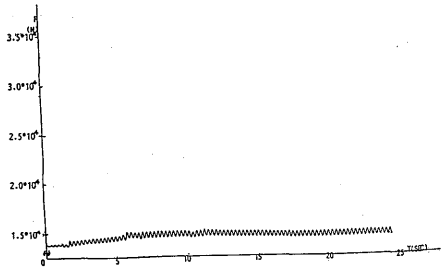

Fig. 6.3 (e) Time history of the amount of pressure on the wall under horizontal vibration. (400 gal, 3.6 Hz, μ_S: 1.0, μ_D: 0.5)

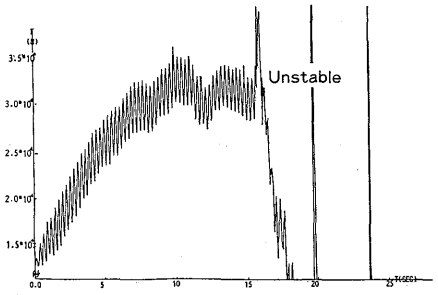

Fig. 6.3 (f) Time history of the amount of pressure on the wall under horizontal vibration. (400 gal, 3.6 Hz, μ_S: 0.2, μ_D: 0.2)

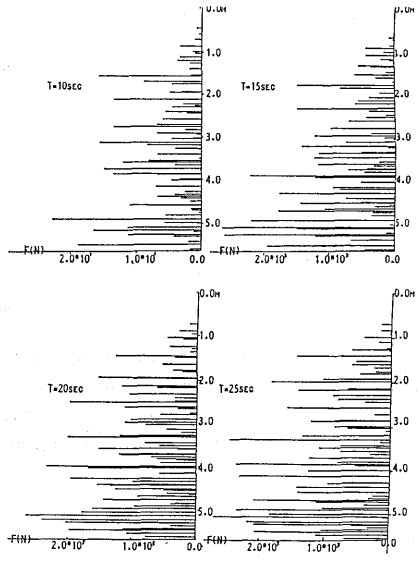

Fig. 6.4. Particles pressure on the wall under horizontal vibration. (400 gal, 3.6 Hz, μ_S: 0.5, μ_D: 0.2)

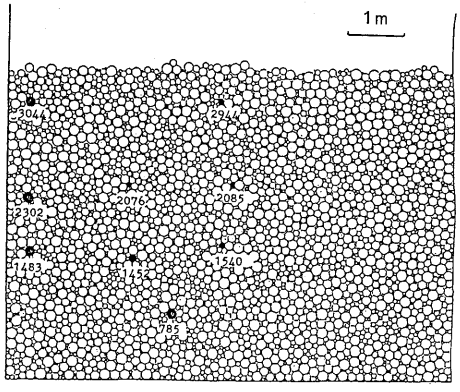

Fig. 6.5. Nine particles to study the the loci.

particles can be deducted from the following.

Particles subsidence starts when the shaking starts and the subsidence volume is large for the small values of friction coefficient (case 12 as an example.) Subsidence of particles and the resultant increase of earth pressure rarely occur when there is a large value of friction coefficient (1.0 in case 1). In any case when particles begin to subside, the acting forces of particles on the wall begin to increase at the upper part of the wall. Forces move downward with the progress of time. The above phenomena are detected from the velocity distributions in Figs. 6.7 and 6.8. It means that particles' movement starts from the upper part of the model, where the normal forces between particles are small, and proceeds downward.

Experiments show that during 25 seconds of shaking, the mean value of the particles' pressure stops increasing 10 seconds after the shaking starts. The mean value of particles' pressure on the wall seems not to be dependent on the amplitude of shaking acceleration. Such a halt of increasing in the mean value of the particles' pressure is caused by the stop of particles' subsidence.

The aforementioned result was achieved considering the subsidence compaction of soil particles that had never been treated by the conventional methods. It is disclosed that the subsidence compaction has much influence on the dynamic earth pressure under the shaking ex-

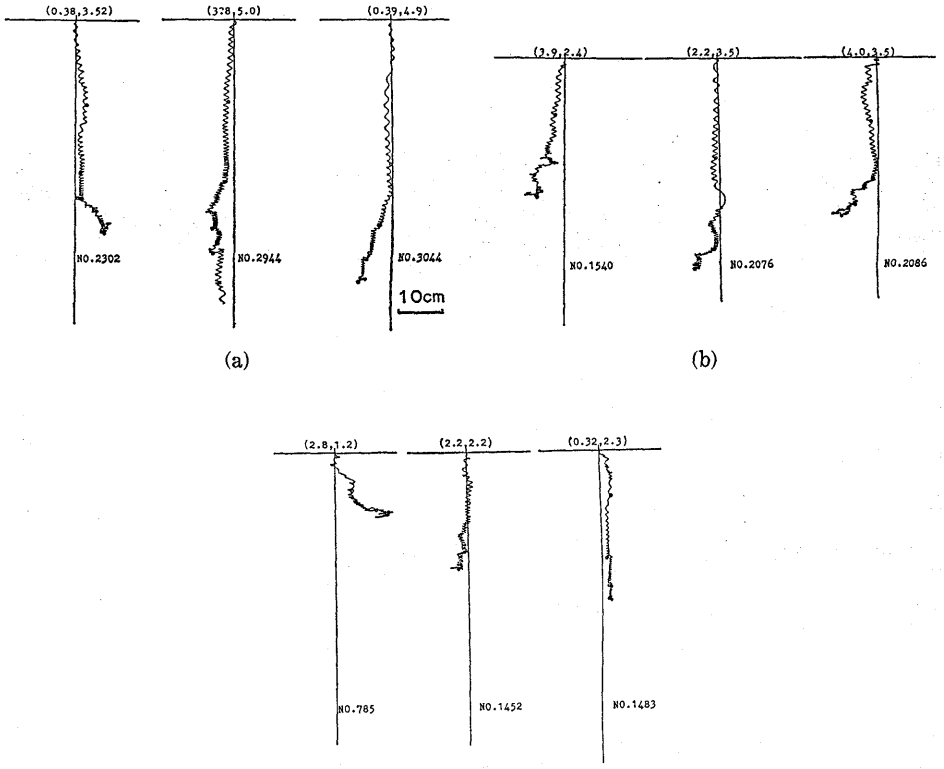

Fig. 6.6. Loci of particles during vibration.

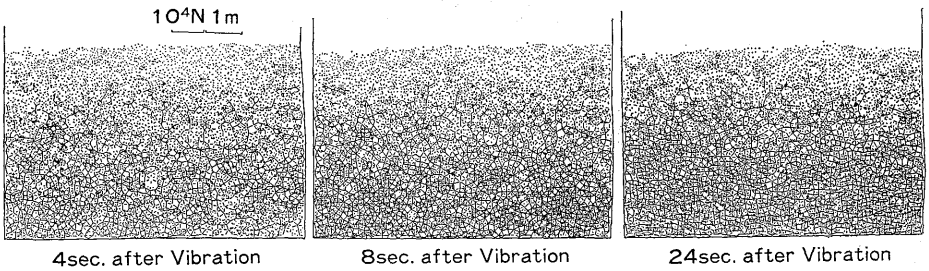

Fig. 6.7. Normal force between particles during vibration.

citation. It makes the earth pressure three times greater than the usual static pressure in the case of loose soil.

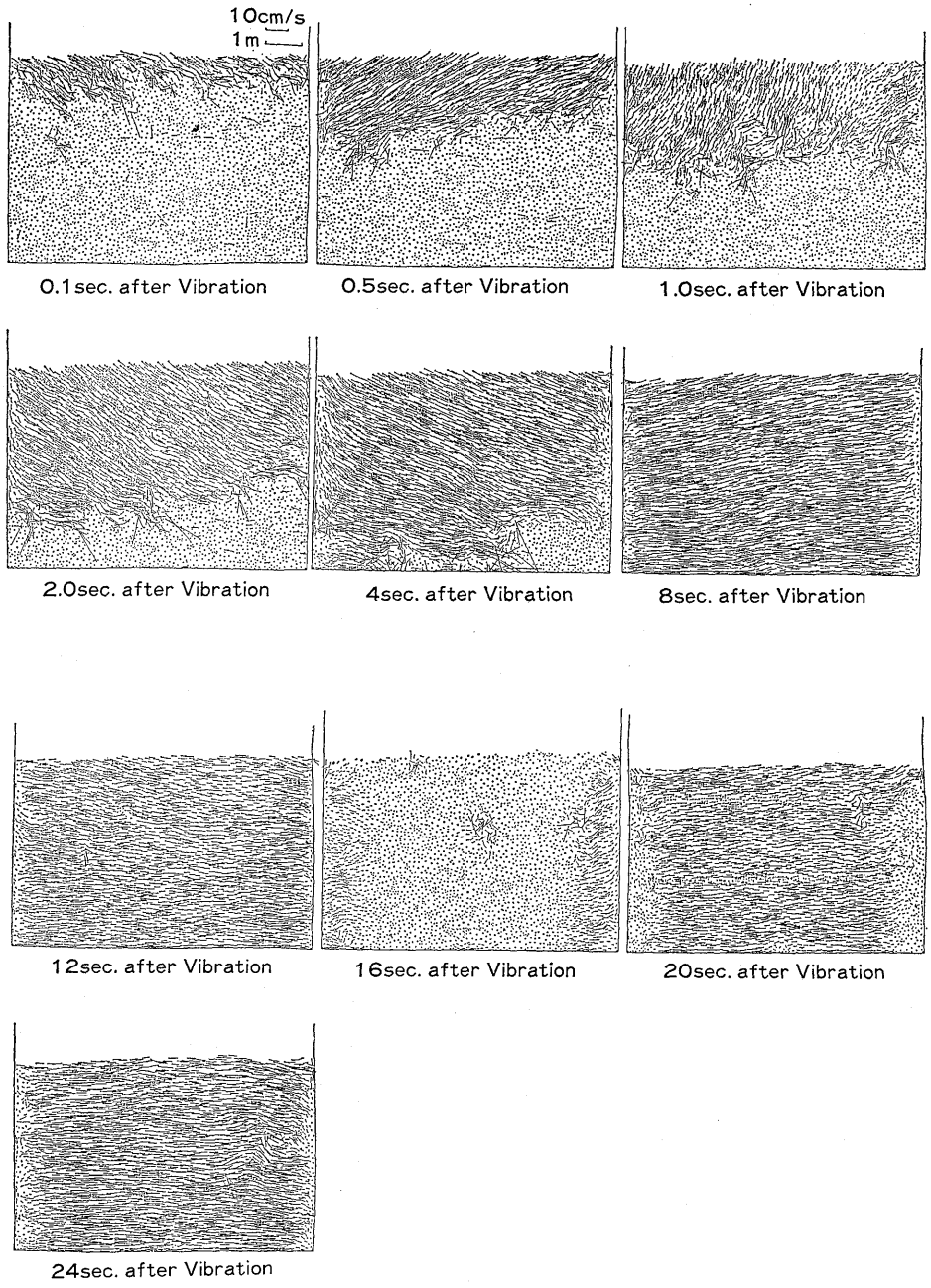

Fig. 6.8. Velocity distribution of particles during vibration.

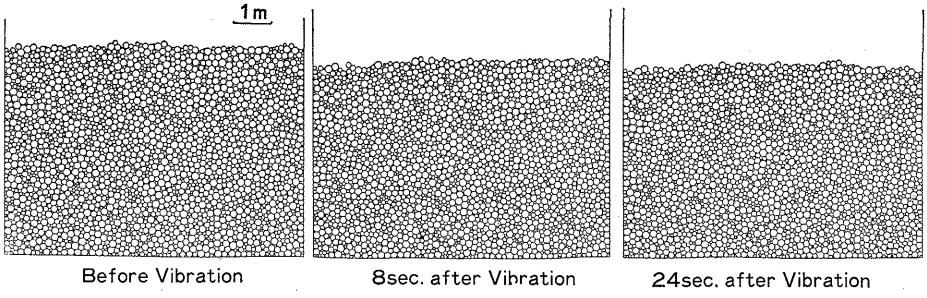

Fig. 6.9. Subsidence of particles during vibration.

7. Conclusion

The authors modified Cundall's DEM (Distinct Element Mothod) and introduced new interpretations. Several simulations related to rock avalanche, penetration of a pile into the ground soil, dynamic properties of a structural foundation and dynamic earth pressure during shaking were performed using the modified DEM.

Those simulations led to the following results as per each interpretation:

1) Rock Avalanche

The large scale rock avalanche occurring on Mt. Ontake due to the Naganoken Seibu earthquake in 1984 was studied as an example. It is disclosed that rock particles of Mt. Ontake collapsed slope slid down in a long period sinusoidal wave form with a speed of approximately 200 km/h. This simulation can be applied also to analyze the behavior of landslides or snowslides.

2) Penetration of a Pile into Ground Soil

It become clear from this study that both the direction and the distance of the movement of soil particles during pile penetration depend on the stage of penetration, their distance from the pile and the slipping zone from the bottom of the pile to the ground surface. The ground surface close to the pile swelled upwards by dilatancy. The penetration simulation was performed using an assembly of 3400 particles. This model could be useful for the analysis of other problems in soil mechanics.

3) Dynamic Fracture of a Structural Foundation embedded in the Ground

In a dynamic response analysis of a structural foundation using the 3,400 particles model, it was clarified that the dynamic response of the structural foundation gives a nonlinear low frequency component. The behavior of the soil surrounding the pile just before the pile fell down was also revealed.

4) Dynamic Earth Pressure on a Retaining Wall under Sinusoidal Excitation

The dynamic earth pressure on a retaining wall with a height of approximately five meters when subjected to seismic loading conditions was analyzed using the same model. This analysis was carried out for various accelerations, frequencies of the input motions and site ground conditions. The dynamic earth pressure became approximately three times greater than before when subjected to 10 seconds of sinusoidal excitation with a maximum acceleration of 800 gal. The increase of earth pressure is not affected by the maximum acceleration but it is affected a little by the shaking frequency. The subsidence of the model ground surface by the excitation was very large and amounted to several tens of centimeters.

Acknowledgements

We are very grateful to Mr. Masahiro Iida (Research Associate in ERI) for his helpful suggestions and continuous encouragement throughout our work. We thank Mr. Kazuyoshi Iwashita (Graduate student in ERI) very much for his kind help on the operation of the computer.

All the computations were made by the computer HITAC M280H in the computer center of the University of Tokyo.

References

ASHIDA K., S. EGASHIRA and H. OHTSUKI, 1982, On the flow mechanism of sliding soil from a mountain slope, *Bull. Disast. Prevention Res. Inst., Kyoto Univ.*, No. 26-B-2, 315–327 (in Japanese).

CUNDALL P. A., 1971, A computer model for simulating progressive, large scale movements in blocky rock system, *Symp. ISRM, Nancy, France, Proc.* 2, 129–136.

CUNDALL P. A. and O. D. L. STRACK, 1979, A discrete numeral model for granular assemblies, *Geotechnique*, **29**, 1, 47–65.

HAKUNO M. and T. HIRAO, 1973, A trial related to random packing of particle assemblies, *Proc. Japan Society of Civil Engineers*, **219**, 55–63 (in Japanese).

KIYAMA H., H. FUJIMURA and T. NISHIMURA, 1982, Analysis on the settlement of ground surface owing to tunnel excavation by Cundall model, *Anual meeting of Japan Society of Civil Engineers*, **3**, 309–310 (in Japanese).

KIYAMA H. and H. FUJIMURA, 1983, Analysis on gravity flow of rock granular assemblies by Cundall model, *Proc. Japan Society of Civil Engineers*, **333**, 137–146 (in Japanese).

粒状体シミュレーションによる地盤の挙動の解析

清水建設 植村大輔
地震研究所 伯野元彦

土とか岩は，砂粒とか土粒子でできていたり，多くの割れ目があったりで，本質的には連続体ではない．勿論，通常の問題では，それ程の大変形が生じる訳ではないので，連続体としての解析で何ら支障はないのであるが，土砂崩壊とか液状化とか，大変形時には無理がある．非連続体の解析手法としては，現在までのところ，有限要素法に滑り要素を導入したものや，有限要素法を多少変えた川井の RBSM 法 (Rigid Body Spring Method), Cundall の DEM 法 (Distinct Element Method) がある．

どの手法にも一長一短があるが，有限要素法の流れを汲む前二者では，要素の辺に沿って滑る変形しかできない，つまり変形方向に制限がある．勿論，断層が滑る場合のように滑る方向が前からわかっている場合には，この方法でよいだろうが，初めて滑る場合などは，大よその破壊形式を推定して，その滑り線に沿って有限要素のメッシュを切ってやらなければならない．一方，Cundall の DEM 法は，要素は元々，バラバラのものとしての取り扱いである．そのバラバラの独立した要素一つ一つについて運動方程式を立てるのであるが，その運動方程式は，通常の剛体の運動方程式である．その方程式の外力の項は，重力によるものと，他要素からのものと，空隙に水などが存在する場合には，それからの圧力とである．他要素からの外力は，二次元の場合接触している他要素が 2 個以下の場合は，算定できるかもしれないが，3 個以上接触している場合は，力の釣合式のみからは求められない．そこで，剛体に法線方向と接線方向のバネをつけ，そのバネの変形から外力を算定する．本研究では，この Cundall の手法を用いて，次のような，種々の土，岩，に関する問題を取り扱った．

i) 岩石崩壊

これは，1984 年長野県西部地震の際の御岳山腹の大崩壊をモデルにして，その様子を模擬したものである．実際に推定されたよりかなり速い粒速度約 200 km/h が得られた．

ii) 杭貫入時の地盤の挙動

杭とかケーソンの形状をした剛体を，地盤を模擬した粒体の中に静的ならびに振動的に貫入した．振動力を加えた方が貫入速度が大きくなったり，杭のそばの地表面が盛り上がるなど，粒状体解析ならではの結果も得られた．

iii) 構造物基礎の振動応答

杭とかケーソンが地中に埋設された状態で，頂部に水平方向の振動力を加えた時の杭，ケーソンの傾き応答を求めた．その結果，加えたモーメントと応答傾角の間に，従来，現場実験でその傾向が得られている，非線形ヒステリシス・カーブが得られた．また，外力は，単調増大正弦波を加えているのに，応答傾角は，或る程度以上大きくなると，一方向にのみ傾角が増大し，振動しないという地震時倒壊を示唆する結果も得られた．

iv) 振動土圧解析

盛土の擁壁が地震時に大丈夫かなどの問題を考える場合，振動時の壁にどのような土圧が加わっているかを知ることは重要である．ゆり込み土圧など，従来，室内実験から得られている結果が本研究によっても求められたばかりでなく，振動による地盤沈下もはっきり認められた．

以上の種々の問題を取り扱って，この手法が，従来の連続体解析では解き得なかったような問題に適用し得ることがわかった．今後，この手法を三次元，液状化解析，コンクリートの破壊解析，地殻の破壊解析などの諸問題に適用して行きたいと思っている．